High Metallicity, Photoionised Gas in Intergalactic Large-Scale Filaments*

Bastien Aracil,¹ Todd M. Tripp,¹† David V. Bowen,² Jason X. Prochaska,³ Hsiao-Wen Chen⁴ and Brenda L. Frye²

- ¹Department of Astronomy, University of Massachusetts, 710 N. Pleasant St., Amherst, MA 01003-9305
- ²Princeton University Observatory, Peyton Hall, Princeton, NJ 08544
- ³University of California Observatories, Natural Sciences II Annex, University of California, Santa Cruz, CA 95064
- ⁴Department of Astronomy & Astrophysics, University of Chicago, Chicago, IL 60637

2 September 2018

ABSTRACT

We present high-resolution ultraviolet spectra of absorption-line systems toward the low-z QSO HS 0624+6907 ($z_{QSO}=0.3700$). Coupled with ground-based imaging and spectroscopic galaxy redshifts, we find evidence that many of these absorbers do not arise in galaxy halos but rather are truly integalactic gas clouds distributed within large-scale structures, and moreover, the gas is cool ($T < 10^5$ K) and has relatively high metallicity $(Z = 0.9 Z_{\odot})$. HST Space Telescope Imaging Spectrograph (STIS) data reveal a dramatic cluster of 13 H I Ly α lines within a 1000 km s⁻¹ interval at $z_{\rm abs}=0.0635$. We find 10 galaxies at this redshift with impact parameters ranging from $\rho = 135h_{70}^{-1}$ kpc to 1.37 h_{70}^{-1} Mpc. The velocities and velocity spread of the Ly α lines in this complex are unlikely to arise in the individual halos of the nearby galaxies; instead, we attribute the absorption to intragroup medium gas, possibly from a large-scale filament viewed along its long axis. Contrary to theoretical expectations, this gas is not the shock-heated warm-hot intergalactic medium (WHIM); the width of the Ly α lines all indicate a gas temperature $T \ll 10^5$ K, and metal lines detected in the Ly α complex also favor photoionised, cool gas. No O VI absorption lines are evident, which is consistent with photoionisation models. Remarkably, the metallicity is near-solar, $[M/H] = -0.05 \pm 0.4$ (2σ uncertainty), yet the nearest galaxy which might pollute the IGM is at least 135 h_{70}^{-1} kpc away. Tidal stripping from nearby galaxies appears to be the most likely origin of this highly enriched, cool gas. More than six Abell galaxy clusters are found within 4° of the sight line suggesting that the QSO line of sight passes near a node in the cosmic web. At $z \approx 0.077$, we find absorption systems as well as galaxies at the redshift of the nearby clusters Abell 564 and Abell 559. We conclude that the sight line pierces a filament of gas and galaxies feeding into these clusters. The absorber at $z_{\rm abs} = 0.07573$ associated with Abell 564/559 also has a high metallicity with [C/H] > -0.6, but again the closest galaxy is relatively far from the sight line ($\rho = 293 \, h_{70}^{-1}$ kpc). The Doppler parameters and H I column densities of the Ly α lines observed along the entire sight line are consistent with those measured toward other low-z QSOs, including a number of broad ($b > 40 \text{ km s}^{-1}$) Ly α lines.

Key words: intergalactic medium — galaxies: abundances — large-scale structure of the universe — quasars: individual (HS0624+6907)

^{*} Based on observations with (1) the NASA/ESA *Hubble Space Telescope*, obtained at the Space Telescope Science Institute, which is operated by the Association of Universities for Research in Astronomy, Inc., under NASA contract NAS 5-26555, (2) the NASA-CNES/ESA *Far Ultraviolet Spectroscopic Explorer* mission, operated by Johns Hopkins University, supported by NASA contract NAS 5-32985, and (3) the Apache Point Observatory

^{3.5}m telescope, which is owned and operated by the Astrophysical Research Consortium.

[†] Visiting Astronomer, Kitt Peak National Observatory, National Optical Astronomy Observatory, which is operated by the Association of Universities for Research in Astronomy, Inc. (AURA) under cooperative agreement with the National Science Foundation.

1 INTRODUCTION

In cold dark matter cosmology, the initially smooth distribution of matter in the universe is expected to collapse into a complex network of filaments and voids, structures which have been termed the "cosmic web". The filamentary distribution of galaxies in the nearby universe has been revealed in detail by recent large galaxy redshift surveys such as the 2dFGRS (Colless et al. 2001, Baugh et al. 2004), the Sloan Digital Sky Survey (SDSS, Stoughton et al. 2002, Doroshkevich et al. 2004) and the $2\mu m$ All Sky Survey (2MASS, Maller et al. 2002). Numerical simulations successfully reproduce this network (Jenkins et al. 1998; Colberg et al. 2004) and indicate that galaxies are only the tip of the iceberg in this cosmic web (Katz et al. 1996; Miralda-Escudé et al. 1996). Hydrodynamic simulations suggest that at the present epoch, in addition to dark matter and galaxies, the filaments are also composed of a mixture of cool, photoionised gas (the low-z remnants of the Ly α forest) and a shock heated, low-density gaseous phase at temperatures between 10⁵ K and 10⁷ K that contains most of the baryonic mass, the "warm-hot" intergalactic medium (WHIM, Cen & Ostriker 1999; Davé et al. 1999).

Observational constraints on the physical conditions, distribution,a nd metal enrichment of gas in the low-redshift cosmic web are currently quite limited. The existence of the WHIM appears to be a robust prediction of cosmological simulations (Davé et al. 2001). Thus, observational efforts are increasingly being invested in the search for WHIM gas and, more generally, the gaseous filamentary structures predicted by the models. Large-scale gaseous filaments have been detected in X-ray emission (Wang et al. 1997; Scharf et al. 2000; Tittley & Henriksen 2001; Rines et al 2001). However, X-ray emission studies with current facilities predominantly reveal gas which is hotter and denser than the WHIM; this X-ray emitting gas is not expected to contain a substantial portion of the present-epoch baryons (Davé et al. 2001). The most promising method for observing the WHIM in the near term is to search for UV (O VI, Ne VIII) and X-ray (O VII, O VIII, Ne IX) absorption lines due to WHIM gas in the spectra of background QSOs/AGNs (Tripp et al. 2000, 2001; Savage et al. 2002,2005; Nicastro et al. 2002; Bergeron et al. 2002; Richter et al. 2004; Sembach et al. 2004; Prochaska et al. 2004; Danforth & Shull 2005). While absorption lines provide a sensitive and powerful probe of the WHIM, the pencil-beam nature of the measurement along a sight line provides little information on the context of the absorption, e.g., whether the lines arise in an individual galaxy disk/halo, a galaxy group, or lower-density regions of a large-scale filament or void.

Thus, to understand the nature of highly ionised absorbers at low redshifts, several groups are pursuing deep galaxy redshift surveys and observations of QSOs behind well-defined galaxy groups or clusters. For example, to study gas located in largescale filaments, Bregman et al. (2004) have searched for absorption lines indicative of the WHIM in regions between galaxy clusters/superclusters and have identified some candidates. In this paper, we carry out a similar search as part of a broader program that combines a large HST survey of low-z O VI absorption systems observed on sight lines to low-z quasars (Tripp et al. 2004) and a ground based survey to measure the redshifts and properties of the galaxies foreground to the background QSOs. The ground based survey is done in two steps: first, multi-band (U,B,V,R and I) imagery is obtained to identify the galaxies and to estimate their photometric redshifts. Then, spectroscopic redshifts are obtained for the galaxies that are potentially (according to the photometric

redhshifts) at lower redshift that the background object. As part of the large HST survey, we have observed the quasar HS0624+6907 ($z_{\rm QSO}=0.3700$) with the E140M echelle mode of the Space Telescope Imaging Spectrograph (STIS) on board the Hubble Space Telescope. We have also obtained multiband images and spectroscopic redshifts of galaxies in the HS 0624+6907 field. The sight line to HS 0624+6907 passes by several foreground Abell clusters (§ 3.1) and provides an opportunity to search for gas in large-scale filaments. We shall show that gas (absorption systems) and galaxies are detected at the redshifts of the structures delineated by the Abell clusters in this direction. While the absorbing gas is intergalactic, and it is likely that we are probing gas in cosmic web filaments, the properties of these absorbers are surprising. Instead of low-metallicity WHIM gas, we predominantly find cool, photoionised, and high-metallicity gas in these large-scale structures.

This paper is organized as follows. The observations and data reduction procedures are described in §2, including HST/STIS and Far Ultraviolet Spectroscopic Explorer (FUSE) observations as well as ground-based imaging and galaxy redshift measurements. In §3, we present information on the foreground environments probed by the HS 0624+6907 sight line, derived from the literature on Abell clusters and from our new galaxy redshift survey. The absorption-line measurement methods are described in §4, and we investigate the physical state and metallicity of the absorbers in §5. Section 6 reviews the properties of the full sample of $Ly\alpha$ lines derived from the STIS spectrum with emphasis on the search for broad $Ly\alpha$ lines. Section 7 discusses the implications of this study, and we summarize our conclusions in §8. Throughout this paper, we use the following cosmological parameters: $h_{70} = H_0/70 \text{ km s}^{-1}$, $\Omega_m = 0.3 \text{ and } \Lambda_o = 0.7$.

2 OBSERVATIONS

2.1 Ultraviolet QSO Spectroscopy

HS 0624+6907 was observed with STIS on 2 Jan. 2002 and 23-24 Feb. 2002 as part of a Cycle 10 HST observing program (ID=9184) . The echelle spectrograph was used with the E140M grating which provides a resolution of 7 km s $^{-1}$ FWHM and covers the 1150-1730 Å range with only a few small gaps between orders at wavelengths greater than 1630 Å. The 0'.2 \times 0''.06 entrance aperture was used to minimize the effect of the wings of the line spread function. The total exposure time was 61.95 ksec. The data were reduced as described in Tripp et al. (2001) using the STIS Team version of CALSTIS at the Goddard Space Flight Center. The final signal-to-noise (S/N) per resolution element is 3 at 1150 Å, increases linearly to 14 at 1340Å and then decreases to 7 at 1730 Å. For further information on the design and performance of STIS, see Woodgate et al. (1998) and Kimble et al. (1998).

HS0624+6907 was also observed by the *FUSE* PI Team on several occasions between 1999 November and 2002 February (Program IDs P1071001, P1071002, S6011201, and S6011202). *FUSE* records spectra with four independent spectrographs ("channels"), two with SiC coatings for coverage of the 905–1105 Å wavelength range, and two with LiF coatings optimized to cover 1100–1187 Å (see Moos et al. 2000,2002 for details about *FUSE* design and performance). The spectrograph resolutions range from 20–30 km s⁻¹ (FWHM). For HS0624+6907, the total integration time in the LiF1 channel was 110 ksec; the other channels had somewhat lower integration times due to channel coalignment problems during some of the observations. We have retrieved the

FUSE spectra from the archive and have reduced the data using CALFUSE version 2.4.0 as described in Tripp et al. (2005). Because the spectra in the individual channels have modest S/N ratios, we have aligned and combined all available LiF channels to form the final spectra that we used for our measurements (we find that combining all available LiF data does not degrade the spectral resolution). For the spectral range uniquely covered by the SiC channels, we used only the SiC2a data. Finally, we compared absorption lines of comparable strength (e.g., Fe II λ 1144.94 vs. Fe II λ 1608.45) observed by FUSE and STIS in order to align the FUSE spectrum with the STIS spectrum and thereby correct the wavelength zero point of the FUSE data.

2.2 Optical Galaxy Imaging and Spectroscopy

One of the primary goals of our low–z QSO absorption line program is to study the connections between galaxies and absorption systems. These studies require good imaging (for galaxy target selection and information on individual galaxies of interest) followed by optical spectroscopy for accurate redshift measurements. To initiate the galaxy-absorber study toward HS 0624+6907 , we first obtained a $10'\times10'$ mosaic of images centered on the QSO with SPICam on the Apache Point Observatory (APO) 3.5m telescope on 2002 October 5. Subsequently, we obtained images of a larger field in better seeing with the NOAO $8k\times8k$ CCD mosaic camera (MOSA, Muller et al. 1998), on the Kitt Peak National Observatory (KPNO) 4m telescope. The SPICam images were used to select targets for the first spectroscopic observing run, but thereafter we only used the better-quality MOSA images.

HS 0624+6907 was observed with MOSA on the 4m on 2003 January 29-30. The field of view is $36' \times 36'$ with a scale of 0'.26/pixel. As summarized in Table 1, images were recorded in U, B, V, R, and I with a standard dithering pattern for filling in gaps between the CCDs and for rejection of cosmic rays. Photometric standard stars from Landolt (1992) were also observed at regular intervals. During these observations, the seeing ranged from 1".0 to 1".3. The data were reduced with the IRAF¹ software package MSCRED following standard procedures. The final R-band MOSA image of HS 0624+6907 is shown in Figures 1 and 2.

Galaxy targets for follow-up spectroscopy were selected from the images using the SExtractor software package (Bertin & Arnouts 1996). Redshifts of 29 galaxies were obtained using the Double Imaging Spectrograph (DIS) on the APO 3.5 m telescope on the following dates: 2002 November 12, 2003 January 29–31, 2003 April 03, 2003 April 21, and 2003 December 25. Spectra were recorded using a single 1.5 arcsec wide slit with total exposure times ranging from 360 to 1800 s per object. The data were processed in the conventional manner, and were wavelength calibrated using helium-neon-argon arc-lamp exposures. Small zero-point offsets in wavelength were applied as needed, after comparing observed skyline wavelengths with their rest values. The spectra were typically recorded at resolutions of $\sim 7-8~{\rm \AA}~{\rm FWHM}.$

The redshift measurements were made following the procedure described by Jenkins et al. (2003). We used the IRAF routine FXCOR to cross-correlate the galaxy spectra with that of the radial velocity standard HD 182572. In general we only used the blue

¹ IRAF is distributed by the National Optical Astronomy Observatories, which are operated by the Association of Universities for Research in Astronomy, Inc., under cooperative agreement with the National Science Foundation. channel DIS data for the cross-correlation, where the 4000 Å break and stellar absorption lines were most apparent. Red channel data were usually used to identify and measure the wavelengths of redshifted emission lines ([O III], H β , H α , etc.) when present. The galaxy redshifts obtained in this way are summarized in Table 2 and are accurate to between 70 and 170 km s⁻¹(which corresponds to a sight line distance displacement uncertainty of 1.0 to 2.4 Mpc for an unperturbed Hubble flow).

We also observed three galaxies with the Echellette Spectrometer and Imager (ESI; Sheinis et al. 2001) on the 10m Keck II telescope on the nights of 2004 September 10 and 11 during morning twilight. We observed galaxy NE3 (see Table 2) in echellette mode with the 0.5" slit which provides $\approx 30~{\rm km~s^{-1}}$ spectral resolution (FWHM). The fainter SE13 and SW3 galaxies were observed in low dispersion mode using a 1" slit which affords $R\sim 2000~{\rm at}$ $\lambda=5000~{\rm Å}$. The exposures were flat fielded and wavelength calibrated with the ESIRedux package (Prochaska et al. 2003^2). The NE3 redshift was derived from the centroids of the high-resolution Na I and H α absorption lines, and the redshift uncertainty is $\sim\!30~{\rm km~s^{-1}}$. For SE13 and SW3, redshifts were measured by fitting Na I, H β , and Ca II H and K, and the uncertainties are $\sim\!150~{\rm km~s^{-1}}$.

The completeness of our galaxy redshift survey (i.e., the percentage of targets brighter than a given magnitude in the SExtractor galaxy catalog with good spectroscopic redshifts) is graphically summarized in Figure 3 as a function of limiting R magnitude and angular separation from the sight line $(\Delta\theta)$. In the $10' \times 10'$ region centered on HS 0624+6907, we have measured spectroscopic redshifts for all galaxies brighter than R = 19.0, and the survey is ≈ 60 per cent complete for R < 20. As we shall see, there is a prominent cluster of absorption lines in the HS 0624+6907 spectrum at $z \approx 0.0635$; at this redshift, 5' corresponds to a projected distance of 367 h_{70}^{-1} kpc, and R = 19.0 corresponds to M = -18.3or L=0.1L* (taking $M_R^*=-21.0$ from Lin et al. 1996). For comparison, the Large Magellanic cloud has a magnitude equal to $M_R = -17$ or L = 0.02L*. At this redshift, we have good completeness even for low luminosity galaxies. At larger radii, a substantial number of bright galaxies are found, and our redshift survey is shallower. Nevertheless, within a 10' radius circle, our survey is still 60 per cent complete for galaxies brighter than R < 19.

3 ABSORBER ENVIRONMENT

Using information gleaned from the literature in combination with our galaxy redshift survey, we can identify several large-scale structures that are pierced by the HS 0624+6907 sight line. In this section we comment on these structures including nearby Abell clusters (§3.1) as well as smaller (and closer) galaxy groups (§3.2).

3.1 Nearby Abell Clusters and Large-Scale Structure

Clusters are clustered and often reveal even larger cosmic structures, i.e., superclusters (Einasto et al. 2001 and references therein). In cosmological simulations, clusters are found at the nodes where large-scale filaments connect. To test the fidelity of cosmological simulations, which are now being used in a wide variety of astrophysical analyses, it is important to search for observational evidence of the expected *gaseous* filaments feeding into clusters

http://www.ucolick.org/~xavier/ESI/index.html

4 B. Aracil et al.

Table 1. Optical Imaging Observations of HS 0624+6907

	Filters						
	U	В	V	R	I		
UT Observation Date Integration Time (s)	2003 Jan. 30 7×900	2003 Jan. 30 6×400	2003 Jan. 29 5×360	2003 Jan. 29 5×360	2003 Jan. 29 5×600		

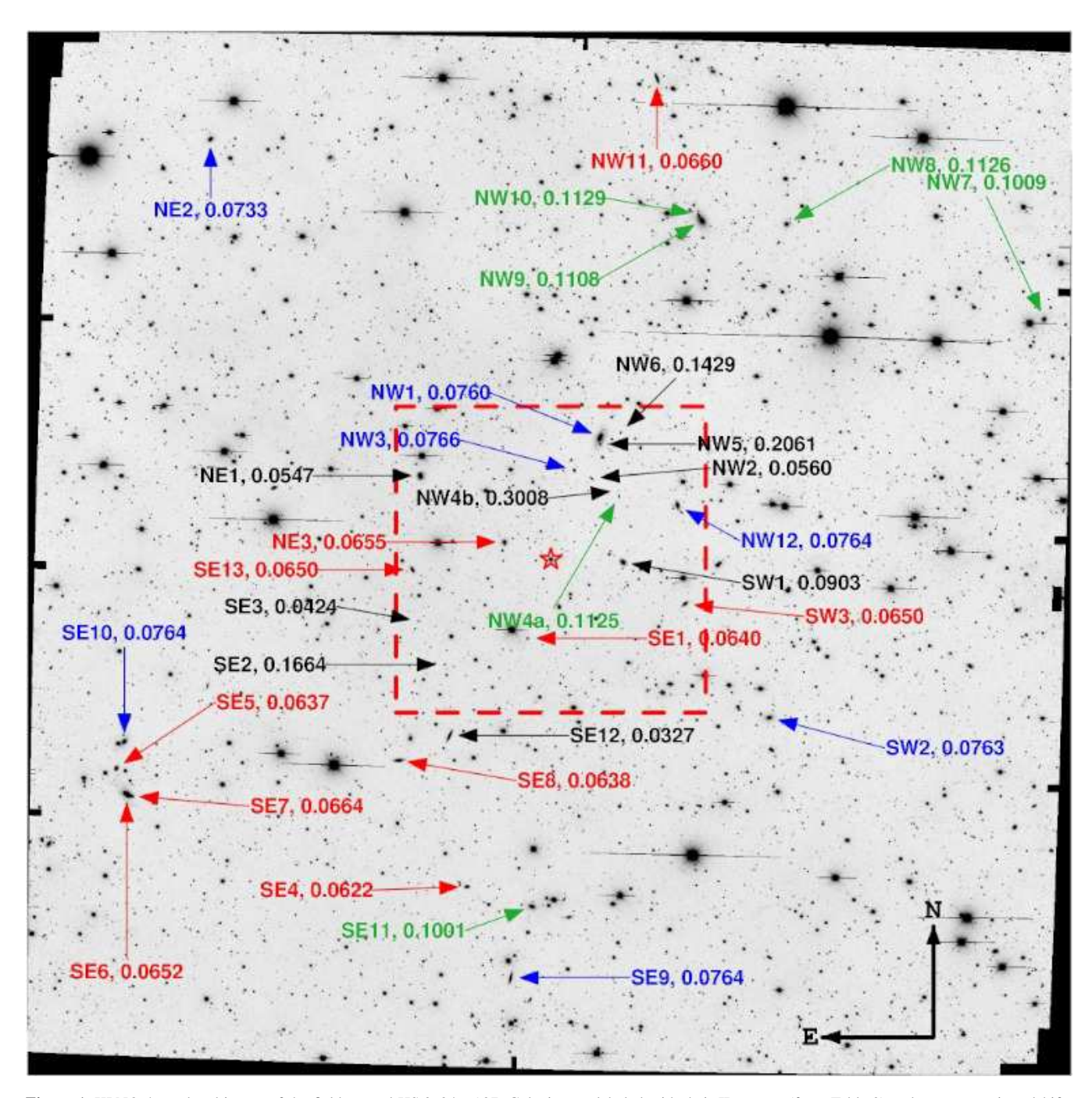


Figure 1. KPNO 4m *R*-band image of the field around HS 0624+6907. Galaxies are labeled with their ID names (from Table 2) and spectroscopic redshifts when available. Theses redshift labels are colour-coded as follows: red for $0.062 \leqslant z \leqslant 0.066$ (10 galaxies), blue for $0.073 \leqslant z \leqslant 0.077$ (7 galaxies), green for $0.100 \leqslant z \leqslant 0.114$ (6 galaxies) and black for the other redshifts. A close up of the $10' \times 10'$ region centered on the QSO (dashed box) is shown in Figure 2.

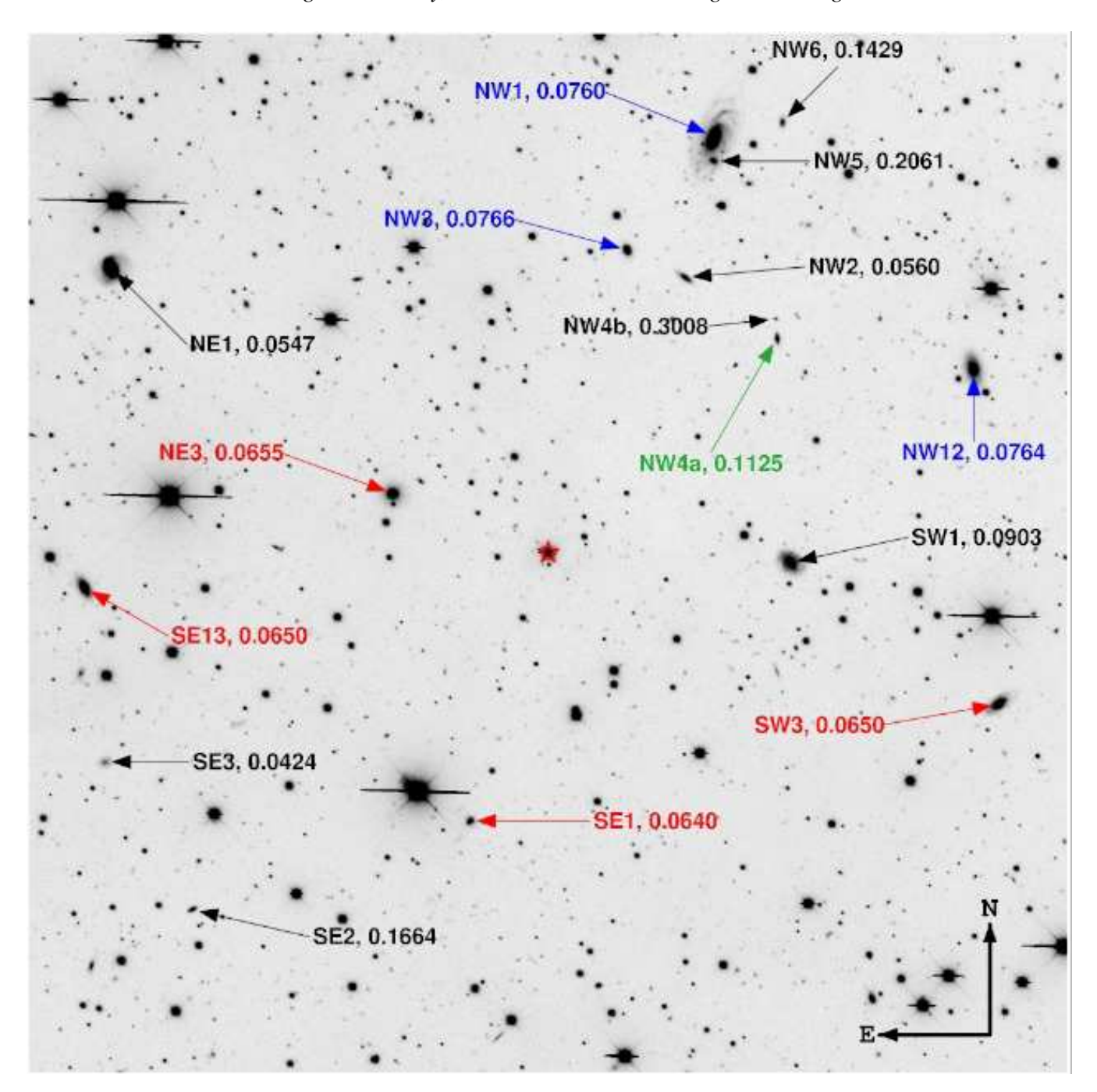


Figure 2. Close-up of the KPNO image shown in Figure 1. This portion of the image shows the $10' \times 10'$ region centered on the QSO and is labeled and colour-coded as described in Figure 1. At redshift $z \simeq 0.065$, 0.076 and 0.11, 10' corresponds to 750, 860 kpc and 1.2 Mpc respectively.

and to measure the properties of the filaments. The sight line to HS 0624+6907 passes through a region of relatively high Abell cluster density and is well-suited for investigation of this topic.

Figure 4 shows the positions of Abell clusters around the sight line to HS 0624+6907, including the cluster richness class and spectroscopic redshift (when available from the literature). The density of Abell clusters in this region is relatively high compared to the vicinity of the other clusters in the Abell catalog: the number of Abell clusters within 2° (3°) of A557 (the cluster closest to the HS 0624+6907 sight line) is 2 (1.6) times larger than the average number within 2° (3°) of all Abell clusters. Einasto et al. (2001)

have identified two superclusters in the direction of HS 0624+6907. Their supercluster SCL71 (at $z\approx 0.110$) includes A554,A557, A561, A562, and A565 while SCL72 (at $z\approx 0.077$) includes A559 and A564. However, A557 and A561 do not have spectroscopic redshifts, and based on our spectroscopic redshifts in the field of HS0624+6907/Abell557 (see Table 2), it appears likely that the visually identified A557 is a false cluster due to the superposition of galaxy groups at several different redshifts. To be conservative, we only use clusters with spectroscopic redshifts to identify large-scale structures. The clusters at $z\approx 0.077$ (A564 and A559) are separated by 4.7 h_{70}^{-1} Mpc from each other, and the clusters

Table 2. Spectroscopic Redshifts of Galaxies in the Field of HS 0624+6907

		Coordinate (J2000)		θ^a	$ ho^b$					
#	ID	RA	DEC	z	(')	$(h_{70}^{-1} \mathrm{Mpc})$	R	V	U - V	M_R
	QSO	06:30:02.50	69:05:03.99	0.3700	0.0	0.000	13.8 ^c	14.2^{c}	0.1^{c}	-27.7 ^c
01	SE12	06:30:41.70	68:58:32.71	0.0327	7.4	0.290	16.6	17.8	1.0	-19.2
02	SE3	06:30:55.32	69:02:41.99	0.0424	5.3	0.265	19.6	20.5	0.9	-16.7
03	NE1	06:30:56.14	69:08:00.90	0.0547	5.6	0.358	15.9	17.0	0.9	-21.0
04	NW2	06:29:46.66	69:08:03.59	0.0560	3.3	0.216	18.6	19.5	0.9	-18.4
05	SE4	06:30:33.00	68:53:02.00	0.0622	12.3	0.887	16.8	17.9	0.9	-20.5
06	SE5	06:32:55.20	68:56:59.99	0.0637	17.4	1.282	16.8	18.3	1.3	-20.5
07	SE8	06:31:01.79	68:57:35.89	0.0638	9.2	0.675	16.0	17.1	0.9	-21.2
08	SE1	06:30:11.22	69:02:09.61	0.0640	3.0	0.222	18.8	19.4	0.7	-18.5
09	SW3	06:29:07.80	69:03:32.01	0.0650	5.1	0.384	17.4	18.3	0.9	-20.0
10	SE13	06:30:58.30	69:04:34.11	0.0650	5.0	0.375	16.9	18.5	1.3	-20.4
11	SE6	06:32:50.70	68:56:03.00	0.0652	17.6	1.318	15.9	17.3	1.2	-21.5
12	NE3	06:30:21.40	69:05:39.70	0.0655	1.8	0.135	16.6	18.1	1.3	-20.8
13	NW11	06:29:23.48	69:22:43.29	0.0660	18.0	1.367	16.3	17.9	1.3	-21.1
14	SE7	06:32:49.20	68:56:00.39	0.0664	17.5	1.334	17.0	18.0	0.7	-20.4
15	NE2	06:32:25.55	69:20:05.81	0.0733	19.7	1.646	16.5	18.0	1.3	-21.1
16	NW1	06:29:43.65	69:09:35.33	0.0760	4.8	0.417	15.9	17.3	1.1	-21.8
17	SW2	06:28:33.03	68:59:26.30	0.0763	9.8	0.849	16.6	18.3	1.3	-21.1
18	SE9	06:30:14.81	68:49:44.79	0.0764	15.4	1.334	16.4	18.0	1.3	-21.3
19	NW12	06:29:11.59	69:07:07.89	0.0764	5.0	0.433	16.4	18.0	1.4	-21.3
20	SE10	06:32:52.40	68:57:59.01	0.0764	16.8	1.457	16.5	18.1	1.3	-21.2
21	NW3	06:29:53.77	69:08:20.51	0.0766	3.4	0.293	18.3	19.6	1.1	-19.4
22	SW1	06:29:33.24	69:05:01.00	0.0903	2.6	0.264	17.1	18.2	0.9	-21.0
23	SE11	06:30:06.84	68:52:22.20	0.1001	12.7	1.407	16.5	18.1	1.2	-21.9
24	NW7	06:26:43.70	69:14:06.91	0.1009	19.9	2.215	16.7	18.2	1.4	-21.6
25	NW9	06:29:03.89	69:17:33.40	0.1108	13.5	1.639	16.4	18.2	1.3	-22.2
26	NW4a	06:29:35.43	69:07:25.80	0.1125	3.4	0.415	18.5	20.2	1.2	-20.1
27	NW8	06:28:29.39	69:17:28.89	0.1126	14.9	1.832	16.7	18.5	1.3	-21.9
28	NW10	06:29:05.25	69:17:46.69	0.1129	13.7	1.685	18.1	19.9	1.3	-20.5
29	NW6	06:29:35.30	69:09:44.99	0.1429	5.3	0.794	19.4	20.4	0.8	-19.8
30	SE2	06:30:44.35	69:01:08.09	0.1664	5.4	0.927	19.3	20.8	1.0	-20.2
31	NW5	06:29:43.52	69:09:19.01	0.2061	4.6	0.927	18.4	20.3	1.4	-21.7
32	NW4b	06:29:35.62	69:07:37.91	0.3008	3.5	0.940	21.0	22.2	0.4	-19.9

Angular separation to the HS 0624+6907 sightline.

at $z \approx 0.110$ (A565, A562 and A554) are separated by 3.9 and 8.7 h_{70}^{-1} Mpc. According to Colberg et al. (2004), in cosmological simulations, more than 85 per cent of the clusters with a separation lower than 10 h_{70}^{-1} Mpc are connected with a filament. We will show in subsequent sections that both absorption lines in the spectrum of HS 0624+6907 and galaxies close to the sight line are detected at the redshifts of both of these Abell cluster structures, which indicates that gaseous filaments connect into the clusters.

3.2 Individual Galaxies and Groups

In this section we offer some brief comments about specific galaxies and galaxy groups close to the sight line of HS 0624+6907, as revealed by our optical spectroscopy. We place these observations in the context of the Abell clusters described in the previous section. We plot in Figure 5 the redshift distribution of the galaxies from Table 2. From this figure we can identify three galaxy groups: two galaxy groups appear to be present at redshifts similar to those of the Abell clusters, i.e, at $z \sim 0.077$ (7 galaxies) and $z \sim 0.11$ (6 galaxies). This indicates that the filament of galaxies connecting A559 to A564 must extend more then 3 degrees (15 h_{70}^{-1} Mpc) west from A559 and structure linking A562 and A554 likely ex-

tends by at least 3 degrees (22 $h_{70}^{-1}~{
m Mpc}$) in order to cross the QSO sight line. However, the most prominent group in Figure 5 includes 10 galaxies at $z \approx 0.064$, which does not match up with any Abell cluster with a known spectroscopic redshift. To show the spatial distribution of galaxies in the three prominent groups in the MOSA field, Figure 6 provides a colour-coded map of projected spatial coordinates of the galaxies. We see that the group at $z \approx 0.064$ is mostly southeast of the sight line while the galaxies associated with Abell 554/562/565 at $z \approx 0.11$ are predominantly northwest of HS 0624+6907. The galaxies associated with the Abell 559/564 $z \approx 0.07$ supercluster appear to extend from the southwest across the sight line to the northeast.

We note that spectroscopic redshifts are not available for several of the clusters shown in Fig. 4, including the one that is closest to the sight line, A557. However, Abell clusters are visually identified without the aid of spectroscopy, and it can be seen from Figures 1 and 6 that several discrete groups are found at the location of A557. It is likely that A557 is not a true cluster but rather is the superposition of several groups in projection.

Is gas also present in these large-scale cosmic filaments? To address this question, we searched the spectrum of HS 0624+6907 for any absorption counterparts at the redshifts of galaxies and

^b Projected distance to the HS 0624+6907 sightline.

 $^{^{}c}$ Due to saturation of the CCD, the magnitudes of the quasar could be underestimated.

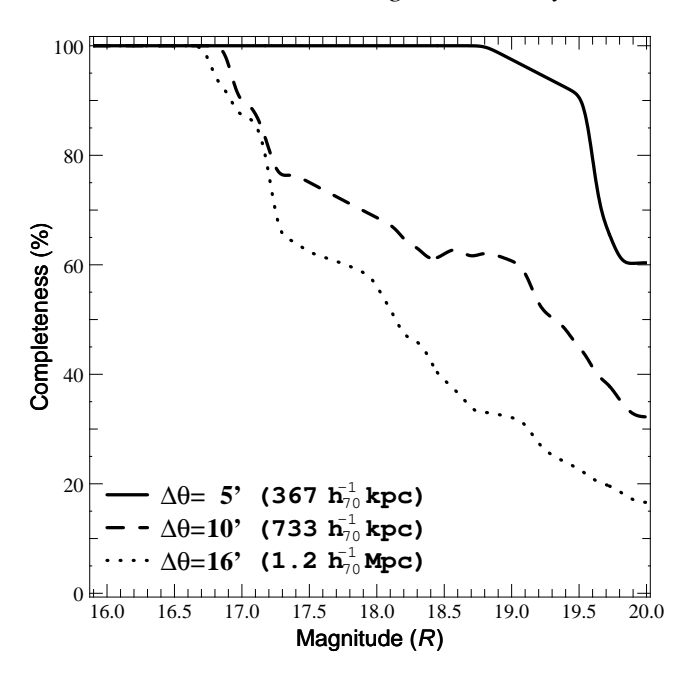


Figure 3. Completeness of the spectroscopic galaxy redshift measurements as a function of limiting R magnitude for targets within an angular separation $\Delta\theta=5$, 10, and 16' as indicated in the key. The key also shows in parentheses the projected physical distances corresponding to these $\Delta\theta$ values at z=0.0635.

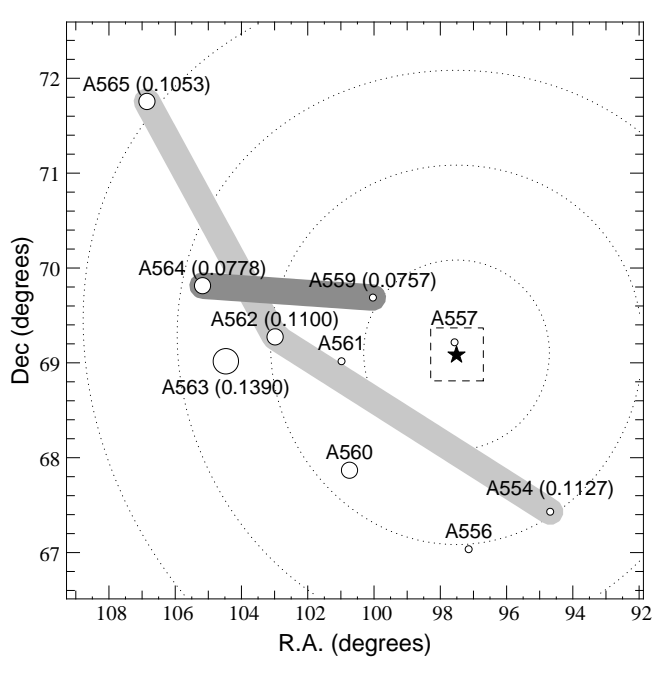


Figure 4. Position of the Abell clusters around the sight line of HS0624+6907. The size of the circles indicates the relative population richness of the cluster. If known, the redshift of the Abell cluster is indicated in parentheses. The shaded regions schematically indicate the possible large scale structures traced by the Abell clusters at $z\approx 0.077$ and $z\approx 0.110$. The dashed rectangle corresponds to the limits of the KPNO image and the star to the position of the quasar. The 1, 2, 3 and 4 degrees angular separation to the quasar are shown by the dotted circles. At redshift $z\simeq 0.076$ and 0.110, 2 degrees correspond to 10 and 14 Mpc respectively.

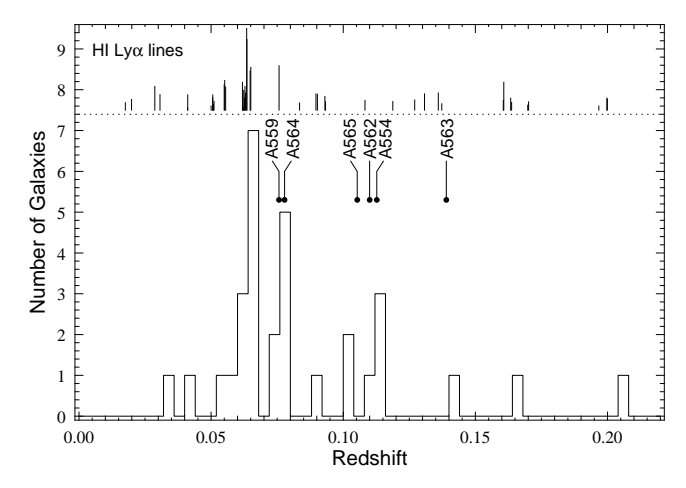


Figure 5. Histogram of galaxy redshifts in the field of HS 0624+6907. H I Lyman- α systems are indicated on the top of the figure with a line height proportional to the absorption line rest equivalent width. Also reported on the figure are the known redshifts of the Abell clusters shown in Figure 4.

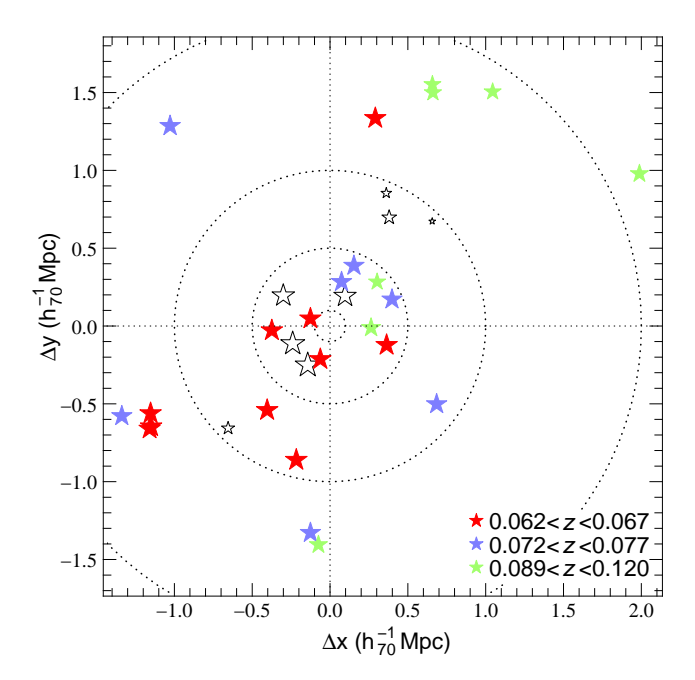


Figure 6. Map of the galaxy distribution around the quasar HS 0624+6907 in projected physical coordinates (north is up and east is to the left). The QSO is at (x,y) = (0,0), and the galaxies with spectroscopic redshifts (see Table 2) are shown with stars. The symbol size is inversely proportional to redshift. Some galaxies are colour-coded by redshift in ranges of z which correspond to peaks in the redshift distribution shown in Figure 5 or the redshifts of nearby Abell clusters (Figure 4). Distances of 0.1, 0.5, 1.0 and $2.0 \ h_{70}^{-1}$ Mpc to the quasar are indicated by dotted circles.

galaxy structures near the QSO sight line. The redshifts of the H I Ly α systems that we have identified and measured (see $\S 4)$ in the spectrum of HS 0624+6907 are plotted at the top of Figure 5; the length of the line is proportional to the rest equivalent width of the Ly α line. This search has revealed three interesting results: First, when a galaxy is located at an impact parameter $\rho \lesssim 500~h_{70}^{-1}~{\rm kpc}$ from the sight line, Ly α absorption is almost always found within a few hundred km s $^{-1}$ of the galaxy redshift (compare Table 2

to Table 3), consistent with the findings of previous studies (e.g., Lanzetta et al. 1995; Tripp et al. 1998; Impey et al. 1999; Chen et al. 2001; Bowen et al. 2002; Penton et al. 2002). Second, strong absorption is clearly detected at the redshift of the $z\sim0.07$ Abell 564/559 supercluster. This absorption system is detected in Ly α , Ly β , and the C IV $\lambda\lambda$ 1548.20, 1550.78 doublet (§5.2), and the absorption redshift is very similar to that of A559. Weak Ly α absorption is also detected at $z_{\rm abs}=0.10822$, which is within 500 km s⁻¹ of the Abell 554/562/565 filament. Evidently, and not surprisingly, gas is also found in the filaments that feed into the clusters near HS 0624+6907. Third, Figure 5 qualitatively indicates that the strongest Ly α lines are situated in the regions of highest galaxy density, which is similar to the conclusions of Bowen et al. (2002) and Côté et al. (2005).

Could these Ly α absorbers simply arise in the halos of individual galaxies? As we show in the next section, the strong H I system at $z_{\rm abs} \approx 0.064$ is comprised of a large number of components spread over 1000 km s⁻¹. Such kinematics are unprecedented in single galaxy halos. In addition, we find no obvious pattern that shows a connection between individual Ly α lines and individual galaxies in this complex. In the case of this strong H I system at $z_{\rm abs} \approx 0.064$, the closest observed galaxy to the sight line around this redshift has $\rho=135\,h_{70}^{-1}{\rm kpc}$ (NE3 in table 2). However, a closer and fainter galaxy could have been missed by the spectroscopic survey. Using photometric redshifts (measured as described in Chen et al. 2003) to cull the distant background galaxies with photometric redshifts > 0.2, we find that there are only four galaxies closer to the sight line than NE3 that could be near $z \approx 0.064$. These four objects are only candidates since photometric redshifts have substantial uncertainties. However, if we assume the redshift of these candidates to be z = 0.064, the closest one to HS 0624+6907 has still a large impact parameter $\rho = 85 h_{70}^{-1}$ kpc. In the case of Ly α at $z_{\rm abs}$ = 0.07573, the closest galaxy in projection is NW3 at $\rho=293\,h_{70}^{-1}$ kpc. It is conceivable that this absorption originates in the large halo of this particular galaxy, but we note that three galaxies are found at $\rho \leqslant 500 \, h_{70}^{-1}$ kpc at this z, and many other origins are possible (e.g., intragroup gas or tidally stripped debris). Finally, the absorption at $z_{\rm abs}=0.10822$ is at a substantial distance (415 h_{70}^{-1} kpc) from the nearest known galaxy (NW4a) and is unlikely to be halo gas associated with that object.

4 ABSORPTION LINE MEASUREMENTS

We now turn to the absorption-line measurements. As discussed in the previous section, Figure 5 compares the distributions of galaxies and Ly α lines in the direction of HS 0624+6907. We have measured the column densities and Doppler parameters of the Ly α lines in the spectrum of HS 0624+6907 using the Voigt profile decomposition software VPFIT (see Webb 1987³). Table 3 summarizes the H I equivalent widths, column densities, and b-values measured in this fashion (some of the lines are strongly saturated and consequently Voigt profile fitting does not provide reliable measurements; we discuss our treatment of these cases below).

A particularly dramatic cluster of Ly α lines is evident at $z_{\rm abs} \approx 0.0635$ in Figure 5. The portion of the STIS spectrum of HS0624+6907 covering this Ly α cluster is shown in Figure 7. To avoid confusion with galaxy clusters, we will hereafter refer to this group of Ly α lines as a Ly α "complex". This complex contains at

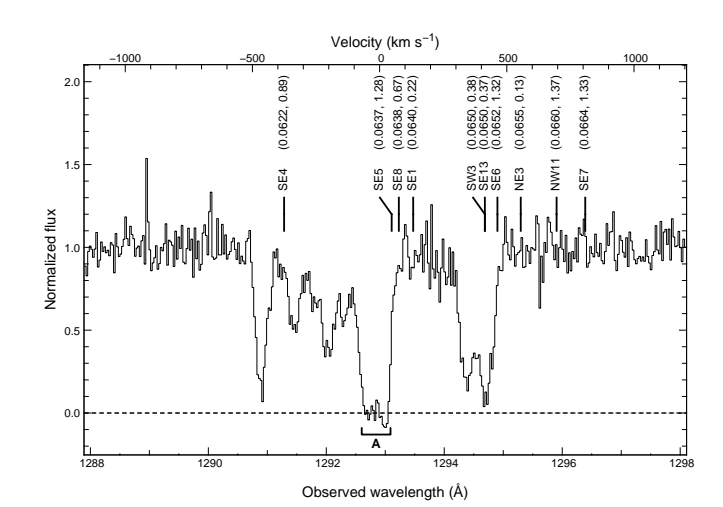


Figure 7. STIS spectrum of HS 0624+6907 between 1288 Å and 1298 Å. All the absorption lines shown are due to a H I Ly α complex covering a velocity range \simeq 1000 km s⁻¹. The velocity of the upper axis is relative to Ly α at z=0.06352. The tick marks show the galaxy redshifts from our spectroscopic survey (§2.2). Apart from the identification name, the labels indicate the redshifts of the galaxies and their projected distances (in h_{70}^{-1} Mpc) from the QSO sight line, respectively.

least 13 H I components spread over a velocity range of 1000 km s⁻¹. We will refer to the strongest Ly α absorption in Figure 7 at $z_{\rm abs} = 0.06352$ as "component A". Component A is detected in absorption in the H I Ly α , Ly β , and Ly γ transitions as well as the Si III λ 1206.50, Si IV $\lambda\lambda$ 1393.76, 1402.77, and C IV $\lambda\lambda$ 1548.20, 1550.78 lines. Low ionisation stages such as O I, C II, and Si II are not detected at the redshift of Component A or at the redshifts of any of the other components evident in Figure 7. The O VI doublet at the redshifts of the Ly α cluster in falls in a region that is partially blocked by Galactic H₂ and Fe II lines. Nevertheless, much of the region is free from blending, and we find no evidence for O VI absorption. We also do not see the N V doublet.

Figure 8 compares the absorption profiles of the Ly α , Ly β , Ly γ , Si III, Si IV, and C IV lines at $z_{\rm abs} = 0.06352$, and Table 4 lists the equivalent widths, column densities, and b-values of the metals detected at this redshift as well as upper limits on undetected species of interest. Both Voigt-profile fitting and direct integration of the "apparent column density" profile (see Savage & Sembach 1991; Jenkins 1996) were used to estimate the metal column densities. These independent methods are generally in good agreement for the metal lines, which do not appear to be strongly affected by unresolved saturation. The Si III $\lambda 1206.50$ absorption at $z_{\rm abs} =$ 0.06352 is slightly blended with a strong H I line at $z_{\rm abs} = 0.05486$ (see Figure 8). However, the metal lines at this redshift have a distinctive two-component profile (see Figures 8 and 11), and the Si III profile shape is in good agreement with those of the C IV and Si IV lines. This indicates that (unrelated) blended Ly α from $z_{\rm abs}$ = 0.05486 contributes little optical depth to the wavelength range where the Si III absorption occurs. We fitted the Si III λ 1206 and H I Ly α at $z_{\rm abs}$ =0.05486 simultaneously, assuming all of the Ly α components are centered shortward of the Si III line. The resulting joint fit is shown in Figure 8.

The profile parameters derived for most of the Ly α lines in the z=0.0635 cluster are reasonably well-constrained. Some of the components are strongly blended and are consequently more uncertain than the formal profile-fitting error bars indicate; these are marked in Table 3. Component A was also difficult to measure

Table 3. Equivalent Widths, Column Densities, and Doppler Parameters of H I Ly α Lines in the Spectrum of HS 0624+6907							
z	W_{obs} (mÅ)	$\log(\mathrm{N})$ (cm ⁻²)	$b \ ({\rm km~s^{-1}})$	z	W_{obs} (mÅ)	$\log(\mathrm{N})$ (cm ⁻²)	$b \pmod{s^{-1}}$
$0.017553 \pm 1.0e-5$	45 ± 10	12.96 ± 0.05	29 ± 4.3	0.207540 ± 0.5 e-5	150 ± 9	13.48 ± 0.02	27 ± 1.5
$0.030651 \pm 0.4e$ -5	99±9	13.36 ± 0.03	22 ± 1.7	$0.213232\pm1.6e-5$	98 ± 14	13.22 ± 0.05	45 ± 5.6
$0.041156 \pm 0.8e-5$	104 ± 11	13.33 ± 0.03	41 ± 3.0	$0.219900 \pm 2.3e-5$	143 ± 15	13.39 ± 0.05	60 ± 8.6
$0.053942 \pm 0.6e$ -5	85 ± 7	13.26 ± 0.04	24 ± 2.3	$0.223290 \pm 0.3e$ -5	256 ± 12	13.86 ± 0.02	25 ± 0.9
$0.054367 \pm 4.1 \text{e-}5^a$	65±13	13.09 ± 0.11	60 ± 19.2^{b}	$0.232305 \pm 2.8 \text{e-}5^a$	125 ± 13	13.33 ± 0.08	44 ± 7.7^{b}
$0.054829^{a,c}$	458 ± 10	\sim 14.5 c	\sim 35 c	$0.232547 \pm 2.3 \text{e-}5^a$	44 ± 10	12.86 ± 0.21	24 ± 7.3
$0.055153 \pm 7.8e-5^a$	237 ± 14	13.68 ± 0.17	84 ± 30.7^{b}	$0.240599 \pm 0.6e$ -5	110 ± 10	13.33 ± 0.04	20 ± 2.0
$0.061879 \pm 0.4e$ -5	184 ± 6	13.77 ± 0.03	21 ± 1.4	$0.252251 \pm 1.2e-5$	55±11	12.96 ± 0.06	24 ± 4.2
$0.062014 \pm 1.0e-5$	21 ± 4	12.63 ± 0.17	8 ± 4.7	$0.268559 \pm 2.1e-5$	68 ± 14	13.03 ± 0.05	51 ± 7.2
$0.062150\pm 1.5 e\text{-}5^a$	13 ± 4	12.41 ± 0.22	10 ± 7.9	0.272240 ± 0.6 e-5	37 ± 8	12.80 ± 0.06	12 ± 2.2
0.062343 ± 0.8 e-5 ^a	128 ± 7	13.45 ± 0.05	30 ± 4.0	$0.279771 \pm 1.7e-5^a$	174 ± 13	13.50 ± 0.06	34 ± 4.9
$0.062647 \pm 2.5 e\text{-}5^a$	101 ± 7	13.31 ± 0.14	35 ± 12.3	0.280171 ± 0.7 e- 5^a	576±15	14.32 ± 0.02	43 ± 1.9^{b}
$0.062762 \pm 0.7 \text{e-}5^a$	39 ± 3	12.95 ± 0.28	8 ± 3.7	$0.295307 \pm 0.7e$ -5	309 ± 15	13.80 ± 0.02	42 ± 2.0
$0.062850 \pm 1.2e-5^a$	110 ± 5	13.42 ± 0.14	20 ± 7.0	0.296607 ± 0.9 e-5	203 ± 18	13.54 ± 0.02	52 ± 2.9
$0.063037 \pm 1.4 \text{e-}5^a$	101 ± 6	13.33 ± 0.13	27 ± 8.8	$0.308991 \pm 0.6e-5$	167 ± 12	13.49 ± 0.03	28 ± 1.8
$0.063456 \pm 1.6e-5^a$	569 ± 9	14.46 ± 0.30	48 ± 8.4^{b}	$0.309909 \pm 5.5 e-5^a$	246 ± 18	13.61 ± 0.10	66 ± 12.3^{b}
$0.063481 \pm 1.6e-5^a$	443 ± 6	15.27 ± 0.13	24 ± 5.5	0.310454 ± 8.0 e- 5^a	170 ± 17	13.43 ± 0.33	62 ± 40.3^{b}
$0.063620 \pm 2.7 \text{e-}5^a$	153 ± 4	14.29 ± 0.38	10 ± 5.6	$0.310881 \pm 14.4e-5$	88 ± 16	13.13 ± 0.43	51 ± 27.7
$0.064753 \pm 0.9e-5^a$	257 ± 9	13.87 ± 0.04	33 ± 3.0	$0.312802 \pm 4.4e-5$	257 ± 18	13.65 ± 0.10	54 ± 9.3
0.065016 ± 0.8 e-5 ^a	282 ± 8	13.97 ± 0.04	31 ± 2.7	$0.313028 \pm 1.6e-5$	72 ± 10	13.09 ± 0.24	17 ± 6.8
$0.075731 \pm 0.2e$ -5	292 ± 8	14.18 ± 0.03	24 ± 0.8	$0.313261 \pm 4.7e-5$	244 ± 19	13.62 ± 0.10	55 ± 10.9
$0.090228 \pm 4.2e$ -5	106 ± 12	13.29 ± 0.08	76 ± 13.7	$0.317901 \pm 1.2e-5$	139±18	13.37 ± 0.04	34 ± 3.6
$0.130757 \pm 1.0e-5$	114 ± 9	13.34 ± 0.04	34 ± 3.6	$0.320889 \pm 0.4e$ -5	349 ± 14	13.97 ± 0.02	31 ± 1.2
$0.135966 \pm 3.9e-5$	119 ± 11	13.33 ± 0.10	57 ± 10.7	0.327245 ± 5.0 e- 5^a	316 ± 21	13.73 ± 0.32	69 ± 15.6^{b}
0.160541 ± 5.0 e-5 ^a	69 ± 7	13.08 ± 0.21	34 ± 10.3	$0.327721\pm38.7e-5^a$	264 ± 26	13.61 ± 0.43	115 ± 62.1^{b}
$0.160744 \pm 1.0e-5^a$	200 ± 7	13.66 ± 0.05	30 ± 2.4	$0.332674 \pm 1.1e-5$	202 ± 18	13.55 ± 0.04	38 ± 3.4
$0.199750 \pm 0.6e$ -5	87 ± 9	13.24 ± 0.05	17 ± 2.0	$0.339759 \pm 0.3e-5$	647 ± 13	14.45 ± 0.03	42 ± 1.3
$0.199946 \pm 1.2e-5^a$	83±11	13.17 ± 0.06	26 ± 4.6	0.346824 ± 0.6 e-5	221 ± 16	13.59 ± 0.02	39 ± 1.9
$0.204831 \pm 0.3e$ -5	208 ± 9	13.72 ± 0.02	24 ± 1.0	0.348645 ± 0.9 e-5	40 ± 10	12.78 ± 0.06	18 ± 3.0

Table 3. Equivalent Widths, Column Densities, and Doppler Parameters of H I Ly α Lines in the Spectrum of HS 0624+6907

 25 ± 0.8

for a different reason: the three usable Lyman series lines (Ly α , Ly β and Ly γ) are all saturated, and consequently Voigt profile fitting did not provide good constraints for the determination of the component A H I column densities. As shown in Figure 9, using a single-component curve of growth and the observed equivalent widths of Ly α , β , and γ , we find that the component A H I absorption lines can be reproduced by two distinct sets of values for the H I column density and the Doppler parameter. One of the two sets implies N(H I) $\sim 10^{17.4}$ cm⁻², which should produce a strong absorption edge characteristic of a Lyman Limit System (LLS) at an observed wavelength of 970 Å. This wavelength region is covered by the *FUSE* spectrum in the SiC2a channel and is shown in Figure 10. The S/N of the SiC2a channel is low but is adequate to constrain $N(H\ I)$. The optical depth $\tau(\lambda)$ of the Lyman limit absorption and the H I column density are approximately related by

 322 ± 8

 14.12 ± 0.03

 $0.205326 \pm 0.2e-5$

$$N({\rm H~I}) = \frac{\tau(\lambda)}{\sigma(\lambda)} = 1.6 \times 10^{17} \left(\frac{912 \rm \mathring{A}}{\lambda}\right)^3 \tau(\lambda) \ {\rm atoms~cm^{-2}(1)}$$

where $\sigma(\lambda)$ is the absorption cross section and λ is the rest-frame wavelength. The SiC2a spectrum does not show any compelling evidence of a Lyman limit edge at the expected wavelength, but the

continuum placement is somewhat uncertain and because of this, a small Lyman limit decrement could be present. Based on the small depth of the flux decrement at $\lambda_{\rm obs}=970$ Å, we derive a 3σ upper limit of $N({\rm H~I})\leqslant 10^{16.1}~{\rm cm}^{-2}$ (upper black solid curve in Figure 10). We also show in Figure 10 the Lyman limit absorption expected for $N({\rm H~I})=10^{16.7}~{\rm cm}^{-2}$ (lower black curve), which is too strong with our adopted continuum placement. The absence of a strong Lyman limit edge rules out the higher H I column density of $10^{17.5}~{\rm cm}^{-2}$ predicted by the curve of growth shown in Figure 9. The lower $N({\rm H~I})$ derived from the curve of growth ($10^{15.4}~{\rm cm}^{-2}$) is consistent with the lack of a Lyman limit edge. To be conservative, we present below the metallicities derived both from the upper limit $[N({\rm H~I})\leqslant 10^{16.1}]$ and from the somewhat lower best value from the curve of growth shown in Figure 9.

5 IONISATION AND METALLICITY

We next examine the physical conditions and metal enrichment of the absorption systems implied by the column densities and the Doppler parameters obtained from Voigt profile fitting. We concentrate on the absorbers at $z_{\rm abs}$ =0.06352 and 0.0757 because these

a Due to blending, the uncertainties in the line parameters could be larger than the formal uncertainties estimated by VPFIT that are listed in this table.

^b This line is part of a multicomponent fit, i.e., the fit is not a single-component fit to an isolated line. Consequently, there is a greater chance that the large Doppler parameter could be due to a blend of several narrow components instead of thermal broadening.

^C For most high-N(H I) lines, we have fitted multiple Lyman series lines so that the fits are constrained by adequately weak, unsaturated lines. However, in this case, all available lines are strongly saturated, and consequently the line parameters are highly uncertain.

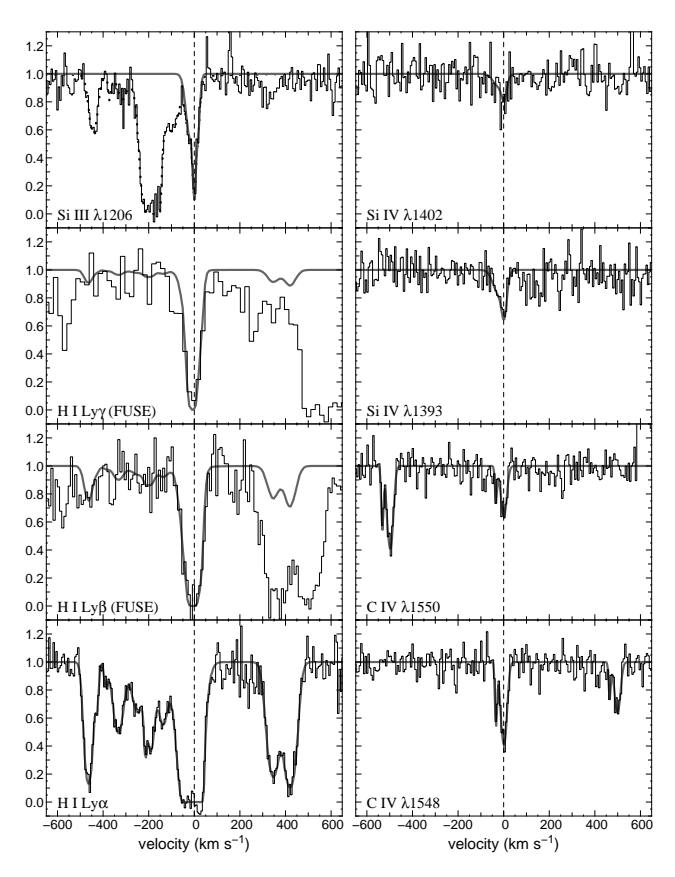


Figure 8. Transitions observed at $z_{\rm abs}=0.06352$ in the spectrum of HS 0624+6907 plotted in the absorber frame ($v=0~{\rm km~s^{-1}}$ at $z_{\rm abs}=0.06352$). The dashed line is centered on "component A", the strongest H I component in the Ly α cluster. The solid line shows Voigt profiles fitted to lines at this redshift; the dotted line indicates fits to unrelated lines at other redshifts. These unrelated lines were fitted in order to deblend the features from the Si III $\lambda 1206.50$ transition.

systems show metal absorption and can be associated with nearby galaxies/structures as discussed in §3. To derive abundances from the detected metals in these systems (Si III, Si IV, and C IV), we must apply ionisation corrections, which depend on the ionisation mechanism and physical conditions of the gas. We will show that the gas is predominantly photoionised, and that the implied metallicities are relatively high.

To investigate the absorber ionisation corrections and metallicities, we employ CLOUDY photoionisation models (v96, Ferland et al. 1998) as described in Tripp et al. (2003). In these models, the absorbers are approximated as constant density, plane-parallel gas slabs with a thickness that reproduces the observed H I column density. The gas in the cloud is photoionised by the UV background from quasars at $z \simeq 0.06$. We used the UV background spectrum shape computed by Haardt & Madau (1996) with the intensity normalized to $J_{\nu} = 1 \times 10^{-23} \text{ ergs s}^{-1} \text{ cm}^{-2} \text{ Hz}^{-1}$ at 1 Rydberg. This value is consistent with theoretical and observational constraints (Shull et al. 1999; Weymann et al. 2001; Davé & Tripp 2001, and references therein). With the models required to match the observed N(H I), the predicted metal column densities depend mainly on the ionisation parameter U (\equiv ionising photon

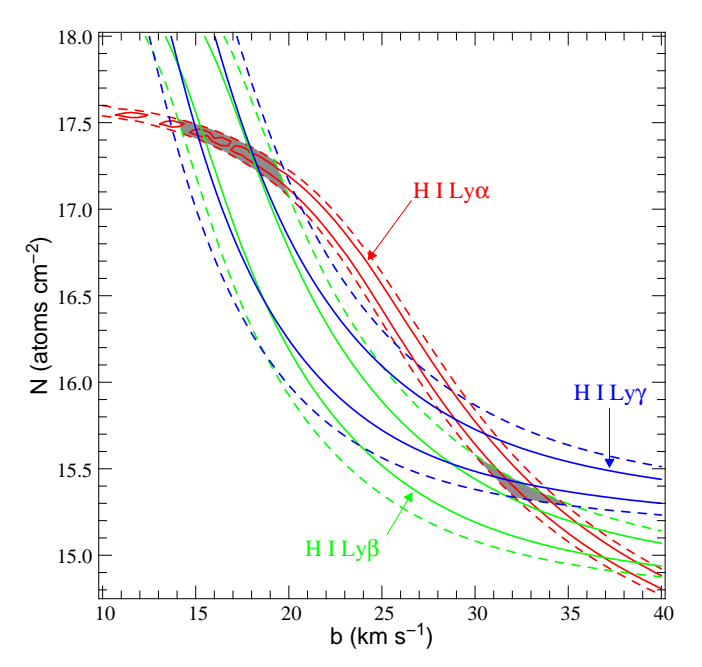


Figure 9. Contour maps of the equivalent width of H I Ly α (in red), Ly β (in green) and Ly γ (in blue) as a function of the column density N and the Doppler parameter b. For each transition, the contours correspond to $W_r \pm 1\sigma$ (solid lines) and $W_r \pm 2\sigma$ (dashed lines). Only the values of b and N in the shaded regions can reproduce the observed equivalent widths for the three transitions.

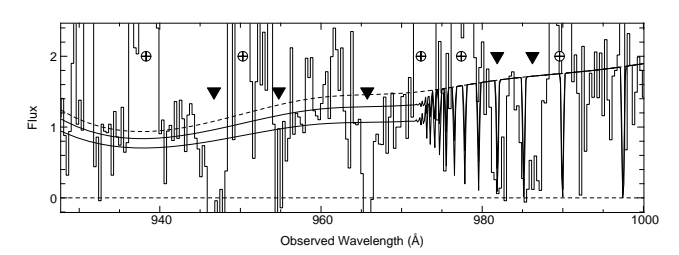


Figure 10. Portion of the HS 0624+6907 *FUSE* spectrum. The data come from the SiC2A channel and are rebinned over 10 pixels. The crossed circles indicate the position of the telluric lines and the black triangles show the position of five strong H₂ absorption features. The dashed curve shows the adopted continuum placement, and the solid curves represent two models of LLS absorption with $N({\rm H~I})$ =10^{16.7} cm⁻² (lower curve) and $10^{16.1}$ cm⁻² (upper curve).

density/total hydrogen number density), the overall metallicity, and the assumed relative abundances of the metals. We assume solar relative abundances, and we adopt recent revisions reported by Allende Prieto et al. (2001,2002) and Holweger (2001) for oxygen, carbon, and silicon, respectively.

The high-ion column densities predicted by the photoionisation models depend on the assumed UV background shape. In this paper, we primarily use the UV background shape computed by Haardt & Madau (1996), but we note that other assessments of the UV background (e.g., Madau, Haardt, & Rees 1999; Shull et al. 1999) adopt a somewhat steeper EUV spectral index for quasars, which changes the CLOUDY ionisation patterns for a given metal-

⁴ In this paper, we express metallicities using the usual logarithmic notation, $[X/Y] = \log (N(X)/N(Y)) - \log (X/Y)_{\odot}$.

Table 4. Equivalents width and column densities of lines at $z \approx 0.06352$

	λ_0		W_{obs}		
Species	(Å)	$\log f \lambda_0^a$	(mÅ)	$\log N_{tot}^{b}$	$\log N_a{}^c$
Н І	1215.670	2.704	603± 9	$15.37^{+0.10}_{-0.16}$	•••
	1025.722	1.909	349 ± 21		
	972.537	1.450	302 ± 22		
O I	1302.168	1.804	6± 9		< 13.1
O VI	1037.617	1.836	28 ± 17		< 13.6
C II	1334.532	2.232	104 ± 9		< 14.3
C IV	1548.204	2.470	$143\pm~9$	13.67 ± 0.04	13.61 ± 0.03
	1550.781	2.169	90 ± 10		13.63 ± 0.05
Si II	1260.422	3.104	23 ± 12		< 12.8
Si III	1206.500	3.304	$151{\pm}10$	$13.02^{+0.24}_{-0.21}$	13.08 ± 0.03
Si IV	1393.760	2.855	76±10	$13.05^{+0.16}_{-0.12}$	12.95 ± 0.06
	1402.773	2.554	49±11		13.05 ± 0.10
N v	1242.804	1.988	23±10		< 13.8

^a Rest wavelengths and f-values are from Morton (1991).

licity and ionisation parameter. We investigate how these UV background uncertainties affect our results by modeling our systems with both UV background shapes (see below).

5.1 $z_{\rm abs} = 0.06352$

As discussed above, the H I absorption lines detected at $z_{\rm abs} = 0.0635$ are spread over a wide velocity range of $\Delta v =$ 1000 km s^{-1} (see Figure 7). From the velocity centroids of the 13 fitted Voigt profiles and by using the biweight statistic as described in Beers et al. (1990), we estimate that the line-of-sight velocity dispersion of this H I absorption complex is $\sigma_v = 265 \text{ km s}^{-1}$. The velocity dispersion of galaxies near this redshift is comparable to this value though substantially more uncertain (due to the larger uncertainties in the galaxy redshifts). This velocity dispersion is comparable to those observed in elliptical-rich galaxy groups (e.g. Zabludoff & Mulchaey 1998), which is interesting because elliptical-rich groups often show diffuse X-ray emission (Mulchaey & Zabludoff 1998) indicative of hot gas in the intragroup medium. However, we will show in §7 that the available information suggests that this group is predominantly composed of late-type spiral and S0 galaxies. Spiral-rich groups are much fainter in X-rays but could still contain hot intragroup gas if the gas is somewhat cooler $(10^5 - 10^6 \text{ K})$ or has a much lower density than that found in elliptical-rich groups (Mulchaey 2000). However, we argue that most of the gas in the Ly α complex at z=0.0635 is unlikely to be hot, collisionally ionised gas for several reasons:

First, the H I lines in the Ly α complex are generally too narrow. If the line broadening is dominated by thermal motions, then the Doppler parameter is directly related to the gas temperature, $b=\sqrt{2kT/m}=0.129\sqrt{T/A}$, where m is the mass, A is the atomic mass number, and the numerical coefficient is for b in km s⁻¹ and T in K. Since other factors such as turbulence and multiple components can contribute to the line broadening, b-values provide only upper limits on the temperature. Applying this equation to the Ly α line b-values from Table 3, we find that most of the H I lines in the z=0.0635 complex indicate that $T\ll 10^5$ K, which is colder than expected for the diffuse intragroup medium based on observed group velocity dispersions, even in spiral-rich

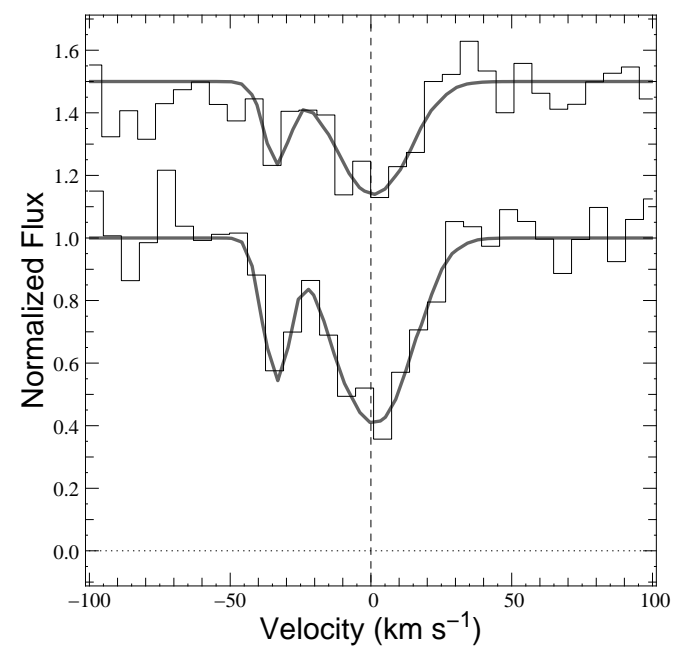


Figure 11. Expanded view of the continuum-normalized C IV $\lambda\lambda$ 1548.20, 1550.78 doublet at $z_{\rm abs}=0.06352$, plotted vs. absorber velocity. In this figure, the data are binned 2 pixels into 1 (i.e., \approx 7 km s⁻¹ pixels). The component at -35 km s⁻¹ is formally found to have $b=4\pm2$ km s⁻¹, which is only marginally resolved at STIS E140M resolution. For clarity, the C IV λ 1550.78 profile is shifted upward by 0.5 flux units.

groups (e.g., Mulchaey et al. 1996). In a complex cluster of $Ly\alpha$ lines, it is easy to hide a broad $Ly\alpha$ component indicative of hot gas (see, e.g., Figure 6 in Tripp & Savage 2000), so the narrow $Ly\alpha$ lines do not preclude the presence of hot gas, but they do indicate that many cool clouds are present in the intragroup medium.

Second, the metal line profiles in component A favor cool, photoionised gas. If component A metal lines were to arise in gas in collisional ionisation equilibrium (CIE), the N(C IV)/N(Si IV)and $N(Si\ IV)/N(Si\ III)$ column density ratios (integrated across both components seen in these species, see Table 4) would require a gas temperature $T \approx 10^{4.9}$ K (Sutherland & Dopita 1993). However the C IV component at $v = -35 \text{ km s}^{-1}$ is rather narrow. To show this, Figure 11 plots an expanded view of the C IV doublet. We see that the $v = -35 \text{ km s}^{-1}$ is marginally resolved at the STIS E140M resolution of $\sim 7~{\rm km~s^{-1}}$. Voigt profile fitting for this component formally yields $b = 4 \pm 2 \text{ km s}^{-1}$, which is significantly lower than the b-value implied by the CIE temperature, i.e., $b \approx 10.5 \text{ km s}^{-1}$. The stronger component at v = 0km s⁻¹ is broader (see Figure 11), but the N(C IV)/N(Si IV) and N(Si IV)/N(Si III) ratios are similar in the components at v=-35and 0 km s^{-1} , and we expect the ionisation mechanism and physical conditions to be similar in both components.

Third, CLOUDY models photoionised by the UV background from QSOs are fully consistent with the measured Si III, Si IV, and C IV column densities (and upper limits on undetected species) at $z_{\rm abs}=0.06352$. Figure 12 shows the relevant metal column densities predicted by CLOUDY models (small symbols connected with solid lines) with log $N({\rm H~I})=15.37$ and $[{\rm M/H}]=-0.05$ compared to the observed column densities (large symbols). We can see that the metal column densities are in agreement (within the 1σ observational uncertainties) with this model at log $U\approx-2.5$ (log $n_{\rm H}\approx-3.9$).

b Sum of the column densities obtained from Voigt profile fitting of the two evident components in the system.

^c Integrated apparent column density $N_a = \int N_a(v) dv$.

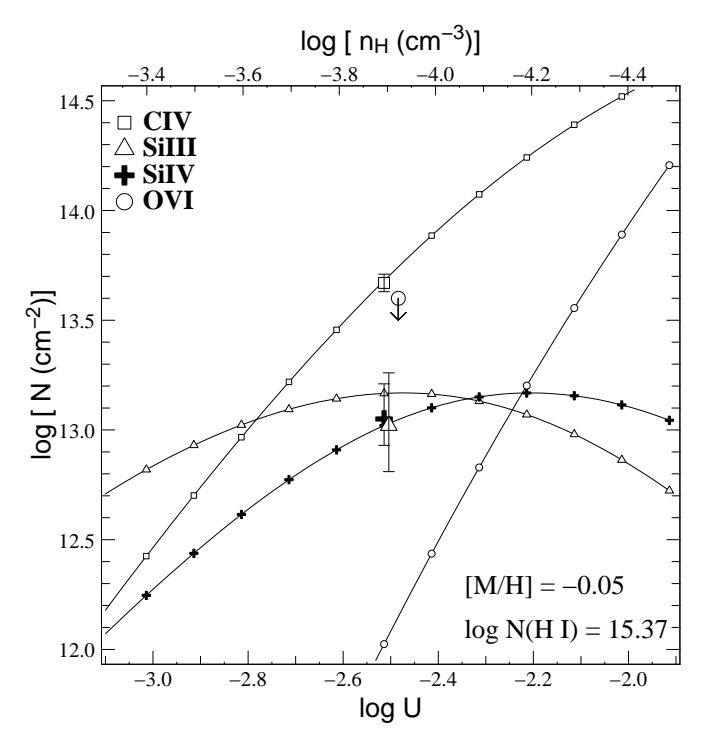


Figure 12. Predicted column densities, calculated with a CLOUDY photoionisation model as described in the text, of O VI (small circles), C IV (small squares), Si IV (small crosses), and Si III (small triangles) as a function of the ionisation parameter U (lower axis) and hydrogen number density $n_{\rm H}$ (upper axis) with $\log N({\rm H~I}){=}15.37$ and nearly solar metallicity ([M/H] = -0.05). The larger markers with 1σ error bars are the observed C IV, Si IV, and Si III column densities measured from the STIS spectrum, plotted with the same symbols at the best-fitting value of U. The 3σ upper limit on $N({\rm O~VI})$ from the FUSE data is indicated with a large open circle.

The narrow H I and C IV components at this redshift could still arise in shock-heated material if they originate in gas that is not in ionisation equilibrium. Many papers have considered the properties of gas that is initially shock-heated to some high temperature and then cools more rapidly than it can recombine (e.g., Shapiro & Moore 1976; Edgar & Chevalier 1986). However, if component A metal lines were to arise in gas in such a state, according to both computations from Shapiro & Moore (1996) and Schmutzler & Tscharnuter (1992), the N(Si III)/N(Si IV) column density ratio would require a gas temperature similar ($T \approx 10^{4.9}$ K) to the one found for the collisional ionisation equilibrium hypothesis. Moreover, assuming solar abundances, the predicted O VI column density at this temperature is always higher than our observed upper limit (\sim 5 times higher in the Schmutzler model). Finally, the N(C IV)/N(Si IV) column density ratio implies an even higher temperature than 10^{4.9} K (2.5 times higherr in the Shapiro model). Because of these points, this non-equilibrium cooling gas scenario seems unlikely to apply to the $z_{
m abs}=0.06352$ absorber toward HS 0624+6907.

The CLOUDY modeling has some other interesting implications in addition to the basic conclusion that the gas is photoionised. For example, the photoionisation model indicates that the absorber has a relatively high metallicity of $Z \simeq 0.9 Z_{\odot}$ even though we have found no luminous galaxies within $\rho \leqslant 135\ h_{70}^{-1}\ \rm kpc.$ A similarly high metallicity ([O/H] $\simeq -0.2$) was recently reported by Jenkins et al. (2005) for a LLS in the spectrum of PHL1811, but that system is much closer in projection to a luminous galaxy.

If we adopt the more conservative upper limit on $N({\rm H~I})$ from the absence of a Lyman limit edge ($N({\rm H~I})=10^{16.1}~{\rm cm}^{-2}$, see Figure 10) instead of the curve-of-growth H I column, we obtain $[{\rm M/H}] \geqslant -0.75$. This lower limit is still substantially higher than metallicities typically observed in analogous absorbers at higher redshifts (e.g., Schaye et al. 2003) and is comparable to abundances seen in high-velocity clouds near the Milky Way (e.g., Sembach et al. 2001,2004; Collins, Shull, & Giroux 2003; Tripp et al. 2003; Ganguly et al. 2005; Fox et al. 2005).

To derive confidence limits on parameters extracted from our CLOUDY models, for combinations of metallicity Z and ionisation parameter U we calculated the χ^2 statistic,

$$\chi^{2}(Z,U) = \sum_{i} \left(\frac{N_{i,obs} - N_{i,model}(Z,U)}{\sigma(N_{i,obs})} \right)^{2}, \tag{2}$$

where N indicates column density and the sum is over the three ions Si III, Si IV, and C IV. With the minimum χ^2 obtained at $[\mathrm{M/H}] = -0.05$ and $\log U = -2.5$, we evaluated confidence limits by finding parameters that increased χ^2 by the amount appropriate for a given confidence level (see Lampton, Margon, & Bowyer 1976; Press et al. 1992). In this way, we find $[\mathrm{M/H}] = -0.05 \pm 0.4$ at the 2σ confidence level. Of course, these confidence limits do not fully reflect potential sources of systematic error such as uncertainties in the shape of the ionising flux field or accuracy of the atomic data incorporated into CLOUDY. When we used the steeper UV background shape (e.g. Madau, Haardt, & Rees 1999; Shull et al. 1999), the observations are still consistent with the CLOUDY model for a lower metallicity of $[\mathrm{M/H}] = -0.24$ and a larger ionisation parameter $\log U = -2.4$.

We can also place constraints on physical quantities such as the absorber size (the length of the path through the absorbing region) and the thermal gas pressure (but see the caveats discussed in §5 of Tripp et al. 2005). Figure 13 shows confidence interval contours for the absorber size L and thermal pressure P/k implied by the photoionisation model. The best fit implies that $L \approx 3.5$ kpc. If spherical, the baryonic mass of this cloud would be $\approx 10^5 M_{\odot}$. However, we can see from Figure 13 that the model allows a large range for L at the 2σ level. The low thermal pressure implied is also notable. When the steeper UV background shape is used for the CLOUDY model, the predicted pressure is lower by a factor 1.5 and the absorber size increases to \simeq 8 kpc. The range of pressures within the contours in Figure 13 is several orders of magnitude lower than the gas pressure measured in the disk of the Milky Way (see Jenkins & Tripp 2001) and is even lower than pressures measured in HVCs in the Milky Way halo (e.g. Wakker, Oosterloo, & Putman 2002; Fox et al. 2005). However, Sembach et al. (1995, 1999) found similar pressure for CIV HVCs surrounding the Milky-Way with somewhat lower metallicity. Moreover, pressures this low are predicted in some theoretical models of galactic halos (Wolfire et al. 1995). Finally, the derived pressure depends on the intensity used to normalize the ionising flux field (see Tripp et al. 2005) and both the particle density and the pressure could be higher if the radiation field is brighter than we assumed.

5.2 $z_{\rm abs} = 0.07573$

As discussed in §3, the absorption lines detected at $z_{\rm abs} = 0.07573$ occur in a large-scale structure connected to A559 and A564. Only H I Ly α , Ly β and the C IV $\lambda\lambda$ 1548.20,1550.78 doublet are clearly detected at this redshift; the profiles of these absorption lines are shown in Figure 14. The weakness of Ly β and the absence of Ly γ

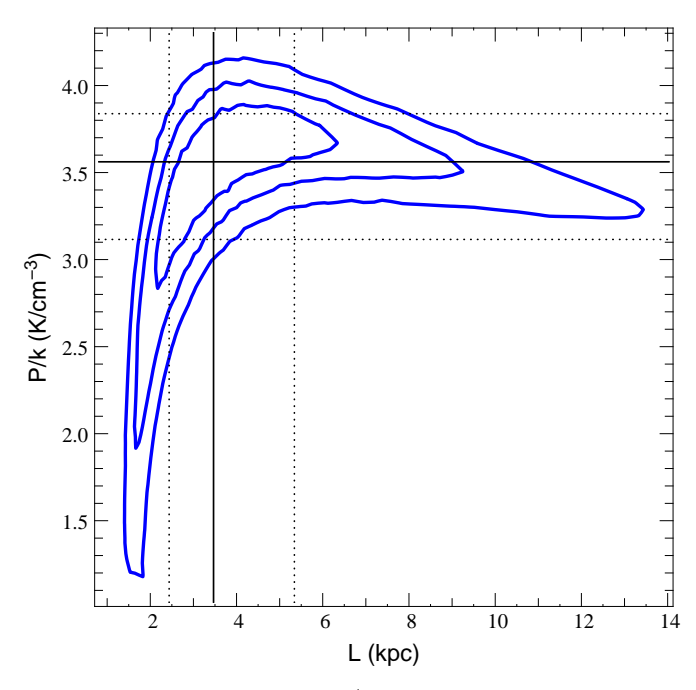


Figure 13. The thermal pressure P/k of the absorber vs. its size L parameter contours at 60, 90 and 99 per cent confidence levels in the joint-fit with the CLOUDY photoionisation modelling. The solid and the dotted black lines indicate for each parameter the best estimation and the 68.7 per cent confidence interval respectively.

suggest that the H I lines are not badly affected by unresolved saturation, and profile fitting measurements are robust. Likewise, comparison of the C IV apparent column density profiles shows no evidence of unresolved saturation. We have fitted these lines with only one component. The results of the fit are listed in Table 5. The width of the H I line ($b=24.6~{\rm km~s^{-1}}$) indicates a temperature for the gas lower than $10^{4.5}~{\rm K}$, which again favors a photoionisation process. No O VI is evident at this redshift, but several strong unrelated lines of various elements are found close to the expected wavelength of the O VI doublet, and these lines might mask weak O VI absorption.

Despite the fact that C IV is the only metal detected in this system, we can nevertheless place an interesting lower limit on the absorber metallicity. The carbon abundance can be expressed as $[{\rm C/H}] = \log[N({\rm C~IV})/N({\rm H~I})] + \log[f({\rm H~I})/f({\rm C~IV})] - \log{({\rm C/H})_{\odot}}$, where $f({\rm H~I})$ and $f({\rm C~IV})$ are the ion fractions of H I and C IV, respectively⁵. With the H I column from the Ly α +Ly β fit (Table 5), and again assuming that the gas is photoionised by the UV background from QSOs (Haardt & Madau 1996), we find that $\log[f({\rm H~I})/f({\rm C~IV})] \geqslant -3.2$, and therefore $[{\rm C/H}] > -0.6$ in the $z_{\rm abs} = 0.07573$ absorber. Once again, this metallicity lower limit is relatively high despite the fact that no luminous galaxies have been found near the sight line (the closest galaxy is NW3 at $\rho = 293h_{70}^{-1}$ kpc, see Table 2).

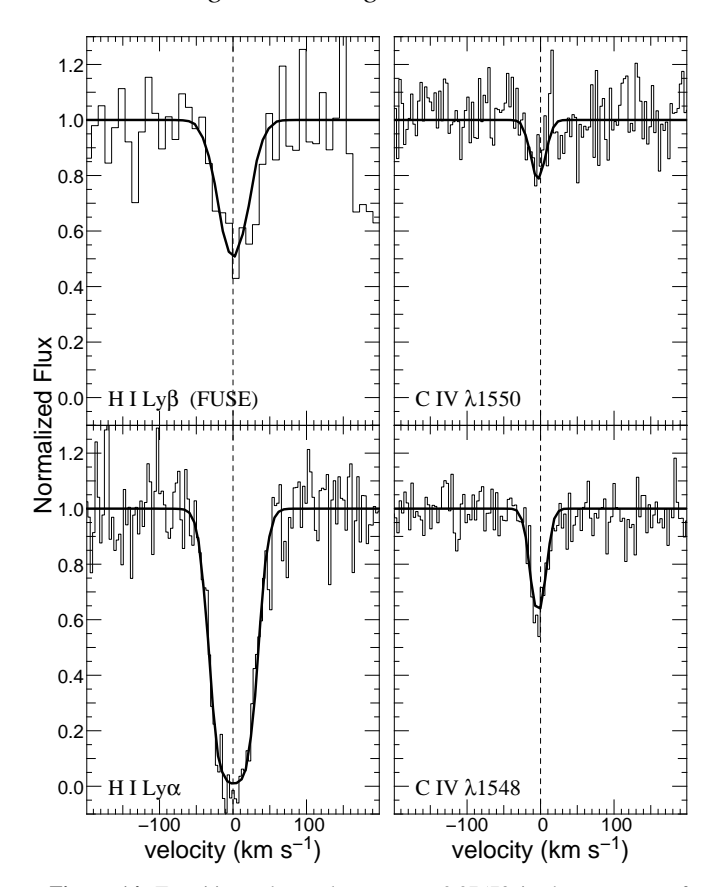


Figure 14. Transitions observed at $z_{\rm abs}=0.07573$ in the spectrum of HS 0624+6907 including H I Ly α , Ly β , and the C IV doublet. The continuum-normalized profiles are plotted vs. velocity in the absorber frame ($v=0~{\rm km~s^{-1}}$ at $z_{\rm abs}=0.07573$).

Table 5. Equivalents width and column densities of detected lines at z=0.07573

	λ_0	W_{obs}		b	
Specie	s (Å)	(mÅ)	$\log N_{tot}$	${\rm km~s^{-1}}$	$\log N_a$
НІ	1215.670	309±10	14.18 ± 0.04	24.6±1.0	14.06±0.03
	1025.722	108 ± 21			14.28 ± 0.08
O VI	1037.617	0 ± 19			< 13.9
C IV	1548.204	51± 7	13.18 ± 0.04	13.1 ± 1.5	13.24 ± 0.04
	1550.781	27 ± 8			12.09 ± 0.22
Si III	1206.500	0 ± 10			< 12.1
Si IV	1393.760	17 ± 14			< 12.8
NV	1238.821	25± 9			< 13.4

5.3 $z_{\rm abs} = 0.113$

In §3 we noted that the clusters A554, A562, and A565 indicate that a large-scale filament/supercluster is foreground to HS 0624+6907. Our galaxy redshift survey has also revealed four galaxies close to HS 0624+6907 at the redshift of the Abell 554/562/565 structure (see Figure 1 and Table 2), which suggests that the large-scale filament extends across the HS 0624+6907 field. However, we only find a couple of weak Ly α lines near the redshift of this structure at redshifts substantially offset from those of the galaxies and Abell clusters. It is possible that the Ly α lines are weak/absent because the gas in the filament is so hot that the H I ion fraction makes the Ly α line undetectable, but we also note that the nearest galaxies are farther from the sight line in this case ($\rho \geqslant 1.2h_{70}^{-1}$ Mpc) than in

⁵ We can derive a lower limit because f(H I)/f(C IV) has a minimum value or, put another way, N(C IV) has a maximum value for any N(H I) and [C/H] combination. The maximum N(C IV) is not evident in Figure 12 because it occurs at a higher value of U than the range shown.

the structures at z=0.064 and 0.077 discussed above, so it is also possible that the sight line does not penetrate the part of the dark matter filament where the potential is deep enough to accumulate gas and galaxies (see discussion in Bowen et al. 2002).

6 COMPARISON TO OTHER LY α ABSORBERS

How do the properties of the Ly α absorbers at 0.064, 0.077, and 0.110 compare to the other Ly α lines in the HS 0624+6907 spectrum (and in other sight lines)? We have found that the systems at 0.064 and 0.077 arise in photoionised cool gas; is this true of the majority of the Ly α lines in the spectrum? In particular, do we find Ly α lines that arise in hot gas? Richter et al. (2004, 2005) and Sembach et al. (2004) have recently identified a population of broad Ly α lines (BLAs) with $b > 40 \text{ km s}^{-1}$ in the spectra of several low-z QSOs (PG0953+415, PG1116+215, PG1259+593, and H1821+643). Williger et al. (2005) similarly find a substantial number of BLAs in the spectrum of PKS0405-123. Bowen et al. (2002) have also identified some BLA candidates using somewhat lower resolution data. If these lines are mainly broadened by thermal motions, then they trace the warm-hot IGM, and moreover, they in this case would contain a substantial portion of the baryons in the Universe at the present epoch (see Richter et al. 2004, 2005; Sembach et al. 2004). Based on simulations, Richter et al. (2005) and Williger et al. (2005) find that some of the BLAs are not predominantly thermally broadened but instead are due to line blends that are difficult to recognize at the S/N afforded by typical STIS echelle spectra. However, Richter et al. (2005) conclude that approximately 50 per cent of the BLAs are mainly thermally broadened, and some high S/N examples in the above papers are remarkably smooth and broad and appear to entirely consistent with a single broad Gaussian (see, e.g., Figures 4 and 5 in Richter et al. 2005).

In this paper, in addition to using a different sight line, we have employed methods that are independent from (e.g., using different software) the techniques used in the papers above for continuum normalization, line detection, and profile fitting. Consequently, we have an opportunity to independently check the BLA findings reported in these papers. For the HS 0624+6907 sight line, we find that the mean b-value for all Ly α lines is $< b>=37~{\rm km~s^{-1}}$, and the median $b_m=33~{\rm km~s^{-1}}$. However, as noted in Table 3, some of the Ly α lines are significantly blended, and the line parameters are accordingly uncertain. If we exclude these uncertain blended cases, we find $< b>=34~{\rm km~s^{-1}}$ and $b_m=30~{\rm km~s^{-1}}$. These ensemble b-values are in reasonable agreement with the previous high-resolution Ly α studies.

In Figure 15 we compare our measurements of the H I b-values and column densities from Table 3 to the measurements reported by Richter et al. (2004) and Sembach et al. (2004). The solid line indicates b vs. N(H I) for a Gaussian line with central optical depth = 0.1. This is effectively a detection threshold; lines that have (b, N) combinations to the left of this line are not likely to be detected. The dotted line in Figure 15 shows the minimum b-value as a function of N(H I) predicted by Davé & Tripp (2001, see their equation 5) from the hydrodynamic cosmological simulations of Davé et al. (1999). This predicted lower envelope appears to be in reasonable agreement with the observed lower envelope for the three sight lines shown in the figure.

From Figure 15, we see that the (b,N) distribution that we have obtained from the HS 0624+6907 sight line appears to be generally similar to those obtained by Sembach et al. (2004) and

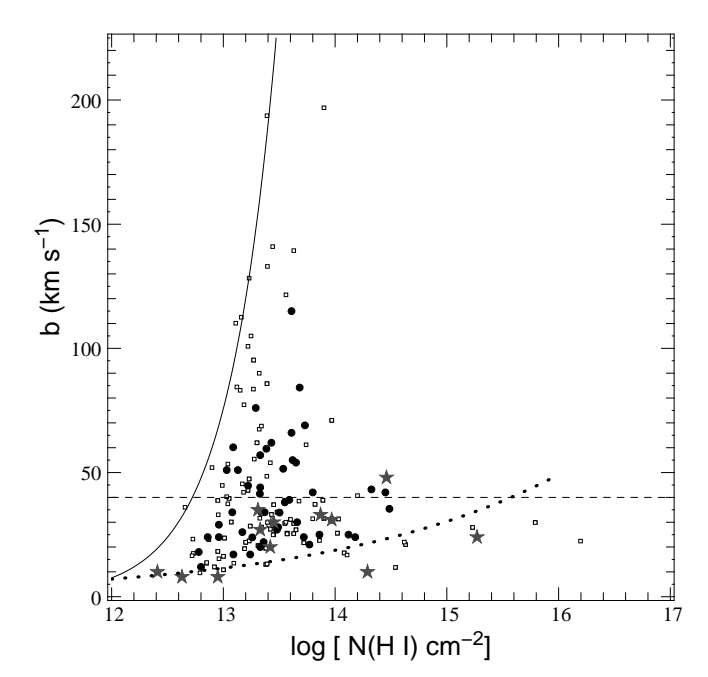


Figure 15. Doppler parameters b as a function of the H I column density N for the $\mathrm{Ly}\alpha$ lines detected in the spectrum of HS 0624+6907 (solid circles, see Table 3). The $\mathrm{Ly}\alpha$ lines detected in the complex at z=0.064 are shown with stars. For comparison, we also plot the measurements from Sembach et al. (2004) and Richter et al. (2004) from the PG1116+215 and PG1259+593 sight lines (open squares). The solid line is the relation between b and N for a $\mathrm{Ly}\alpha$ absorption line with central optical depth =0.1; this represents a detection threshold for these data. The dotted line shows the minimum b-value as a function of $N(\mathrm{H~I})$ predicted by equation 5 of Davé & Tripp (2001), which is based on the hydrodynamic cosmological simulations of Davé et al. (1999). Lines above the horizontal dashed line have $T>10^5$ K if the lines are predominantly thermally broadened.

Richter et al. (2004). Sembach et al. and Richter et al. did find more extremely broad Ly α lines ($b > 80 \text{ km s}^{-1}$) than we have been able to positively identify in the HS 0624+6907 spectrum. This may be partly due to signal-to-noise differences - the data employed by Richter et al. and Sembach et al. have higher S/N - because such broad and shallow lines are difficult to detect in the HS 0624+6907 data. For $40 < b < 80 \text{ km s}^{-1}$, the different sight lines appear to be in broad agreement. Excluding lines within 5000 km s⁻¹ of the QSO redshift,⁶ the HS 0624+6907 spectrum can be used to search for BLAs between $z_{\rm min} = 0.004$ and $z_{\rm max} = 0.347$. Accounting for regions in which broad lines could have been masked by IGM or ISM lines, we obtain a blocking-corrected total redshift path $\Delta z = 0.329$. With 21 Ly α lines in the sample with b >40 km s⁻¹, we thus obtain dN/dz(BLA) = 64±16. This is somewhat larger than the values reported by Sembach et al. (2004) and Richter et al. (2004,2005). However, Richter et al. have excluded BLAs that are located in complex blends on the grounds that these cases are more likely to be affected by non-thermal broadening. If we follow the same procedure, we must reject 10 BLAs (see Table 3); the remaining 11 BLAs would then imply dN/dz(BLA) = 33±10. Using equations 1, 5, and 6 from Sembach et al. (2004), but adjusted for the somewhat different cosmological parameters

 $^{^6}$ Lines within 5000 km s $^{-1}$ of the QSO redshift can arise in intrinsic gas ejected by the QSO, and these lines can be rather broad (see, e.g., Yuan et al. 2002), even if not part of a full-blown broad absorption line outflow.

assumed in this paper, we find that our full sample implies that the BLA baryonic content is $\Omega_b(\text{BLA}) = 0.017 \ h_{70}^{-1}$ (in the usual notation, i.e., $\Omega = \rho/\rho_c$). This high value probably substantially overestimates the BLA baryonic content, largely because of false BLAs that arise from blends. If we exclude BLAs that are located in complex blends, this drops to $\Omega_b(BLA) = 0.0036 \ h_{70}^{-1}$, which is similar to values obtained by Richter et al. and Sembach et al. The uncertainties in $\Omega_b(BLA)$ due to, e.g., lines that are broad due to blends or other non-thermal broadening mechanisms, are large and currently difficult to assess (see discussion in Richter et al. 2005). However, these initial calculations suggest that BLAs may harbor an important quantity of baryons. With future UV spectrographs, it would be valuable to obtain high-resolution spectra with substantially better S/N in order to accurately assess the baryonic content of BLAs as part of the general census of ordinary matter in the nearby Universe.

7 DISCUSSION

We have acquired detailed information about the abundances, physical conditions, and galaxy proximity of absorption systems in the direction of HS 0624+6907. What are the implications of these measurements for broader questions of galaxy evolution and cosmology? The processes that add gas to galaxies (e.g. accretion) and remove gas from galaxies (e.g., winds, dynamical stripping) can have profound effects on galaxy evolution, and the "feedback" of matter and energy from galaxies into the IGM is now believed to play an important role in shaping structures that subsequently grow out of the IGM (Voit G. M., 2005). The quantity and implications of the $10^5-10^7~\rm K$ WHIM gas is a topic of particular interest currently. The galaxies and absorption systems in the direction of HS 0624+6907, particularly the galaxy group and Ly α complex at z=0.064, have some interesting, and perhaps surprising, implications regarding these questions, which we now discuss.

ROSAT observations of diffuse X-ray emission have established that galaxy groups that are dominated by early-type galaxies often contain diffuse, hot intragroup gas (Mulchaey 2000, and references therein). Based on the observed relation between intragroup gas temperature and velocity dispersion σ in X-ray bright groups ($T \propto \sigma^2$) and the fact that spiral-rich groups have lower velocity dispersions than elliptical-rich groups, Mulchaey et al. (1996) have hypothesized that spiral-rich groups might have somewhat cooler intragroup media that could give rise to QSO absorption lines at WHIM temperatures (e.g., O VI).

However, the galaxy group at z = 0.064 appears to have properties that are not consistent with the elliptical-rich groups detected with ROSAT nor with the idea that spiral-rich groups contain warm-hot intragroup gas. It is unclear if the galaxy group at z = 0.064 is a spiral-rich group. Figure 16 shows R images from the MOSA data of the 10 galaxies that we have found in this group. Most of the galaxies in the group show evidence of disks and bulges (both in the direct images and in radial brightness profiles). We find from visual inspection that 4-5 of the 10 galaxies have indications of spiral structure (SW3, SE1, SE8, SE6, and possibly SE4). However, the remaining galaxies could be early-type S0 galaxies, and therefore the early-type fraction might be comparable to groups that show diffuse X-ray emission (see, e.g, Figure 7 in Zabludoff & Mulchaey 1998). The NE3, SE13, and SE5 galaxies, which morphologically appear to be early-type galaxies, have colours and magnitudes consistent with the "red sequence" colour-magnitude relation observed in clusters (e.g., Bower, Lucey, & Ellis 1992;

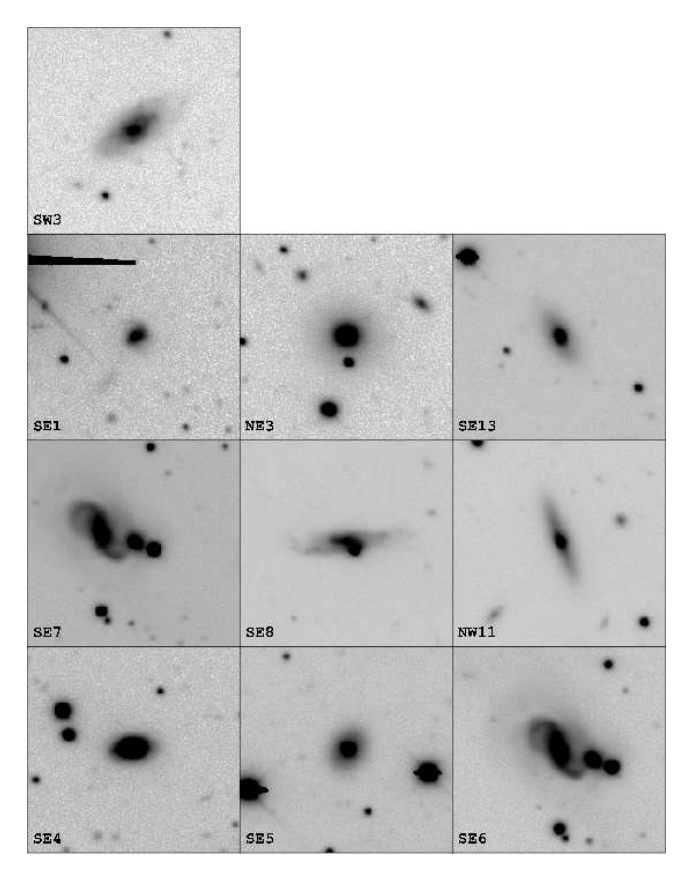


Figure 16. Images of galaxies found in the z = 0.064 group in the field of HS 0624+6907, recorded in the R band with the KPNO 4m MOSA camera. Each box in the montage spans $50'' \times 50''$, and the galaxy name from Table 2 is listed in the lower left corner. The galaxy is in the center of each panel. SE6 and SE7 are in close proximity; SE6 is the more extended spiral galaxy.

McIntosh et al. 2005); these galaxies are likely S0s (the other 7 galaxies have blue colours characteristic of late types). The velocity dispersion of the group at z=0.064, albeit uncertain, is more comparable to those of elliptical-dominated groups than spiral-rich groups (Mulchaey et al. 1996; Zabludoff & Mulchaey 1998).

Regardless of whether the group is elliptical- or spiral-rich, it is surprising that we find a large number of cool, photoionised clouds in the intragroup medium (§5.1). In the hot intragroup medium of an elliptical-rich group, H I lines should be extremely broad and weak, but instead we find strong, narrow lines (see Figure 7). Even in the cooler gas predicted to be found in late-type dominated groups, the H I lines should be broader. We could entertain models of cooling intragroup gas, but in such models O VI is expected to be stronger. Likewise, if the intragroup gas is a multiphase medium with cooler clouds (which cause the H I absorption lines) embedded in a hotter phase, then we might expect to detect O VI from the interface between the phases (Fox et al. 2005), unless conduction is somehow suppressed.

The lack of evidence of hot gas leads us to question whether this group is a bound, virialized system. An alternative possibility is that our sight line passes along the long axis of a large-scale filamentary structure in the cosmic web. In this case, the projection of the galaxies and $Ly\alpha$ clouds along the sight line could give a false impression of a group in which hot gas would be expected. However, in cosmological simulations of large-scale filaments, WHIM

gas is expected to be widespread at the present epoch, even in modest-overdensity regions (see, e.g., Figure 4 in Cen & Ostriker 1999b), so it is interesting that we find a substantial number of cool clouds at $z \approx 0.064$, somewhat contrary to theoretical expectations. As noted above, our data do not preclude the presence of WHIM gas at $z \approx 0.064$, but we find no clear evidence of it. Other sight lines show similar clusters of Ly α lines, e.g., the Ly α complex at $z_{abs} \approx 0.057$ toward PKS2155-304 (Shull et al. 1998; Shull, Tumlinson, & Giroux 2003) or the Ly α lines at $z_{abs} \approx$ 0.121 toward H1821+643 (Tripp et al. 2001). However, unlike the HS 0624+6907 Ly α complex, the PKS2155-304 and H1821+643 examples both show evidence of warm-hot intragroup gas. To test whether the observations and simulations are in accord, it would be useful to assess the frequency and physical properties of these Ly α complexes in cosmological simulations for comparison with the observations.

It is also interesting that the two systems for which we have obtained abundance constraints (at z=0.064 and 0.077) both indicate relatively high metallicities, but both of these systems are at least 100 kpc away (in projection) from the nearest known galaxy. This naturally raises a question: how did gas that is so far from a galaxy attain such a high metallicity? The gas could have been driven out of a galaxy by a galactic wind; some wind models predict that the outflowing material will have a high metallicity (Mac Low & Ferrara 1999), The difficulty with this interpretation is that winds from nearby galaxies are usually observed to contain substantial amounts of hot gas (e.g., Strickland et al. 2004), which seems to be inconsistent with the absorption line properties as we have discussed.

A more likely explanation is that the high-metallicity gas we have detected in absorption has been tidally stripped out of one of the nearby galaxies. There are indications that tidal stripping could be a more gentle process for removing gas from galaxies, and a tidally stripped origin can therefore more easily accommodate the observed low-ionisation state of the gas. For example, in the direction of NGC3783, the Galactic high-velocity cloud (HVC) at $v_{\odot} = 247 \text{ km s}^{-1}$ is now recognized to be tidally stripped debris from the SMC. While this tidally stripped material shows a wide array of low-ionisation absorption lines, it has little or no associated high-ion absorption (Lu et al. 1994; Sembach et al. 2001a). Moreover, the tidally-stripped HVC contains molecular hydrogen, which Sembach et al. argue formed in the SMC and survived the rigors of tidal stripping (as opposed to forming in situ in the stream). Both the absence of high ions and the survival of H₂ suggest that the stripping process did not substantially ionise and heat this HVC. Several galaxies are close enough to the HS 0624+6907 sight line to be plausible sources of the gas in a tidal stripping scenario. One of the nearby galaxies, SE1, has a distorted spiral morphology. This galaxy is a plausible source of tidally stripped matter.

8 SUMMARY

We have presented a study of absorption-line systems in the direction of HS 0624+6907 using a combination of high-resolution UV spectra obtained with *HST/STIS* and *FUSE* plus ground-based imaging and spectroscopy of galaxies within $\sim \! \! 30'$ of the sight line. In addition to presented the basic measurements and ancillary information, we have reported the following findings:

1. There are several Abell galaxy clusters in the foreground of HS 0624+6907, including two clusters at $z\approx 0.077$ (A559 and A564) and three at $z\approx 0.110$ (A554, A562, and A565). These

clusters trace large-scale dark matter structures, i.e., superclusters or filaments of the "cosmic web". Our galaxy redshift survey has revealed galaxies at these supercluster redshifts in the immediate vicinity of the HS 0624+6907 sight line, and therefore our QSO spectra provide an opportunity to study the gas in large-scale intergalactic filaments. The most prominent group of galaxies found in our galaxy redshift survey is at $z\approx 0.064$ and is not associated with an Abell cluster with a spectroscopic redshift from the literature. However, A557, for which no spectroscopic redshift has been reported, is at least partly due to the galaxy group at $z\approx 0.064$.

- 2. The two strongest Ly α absorption systems at z < 0.2 arise in galaxy groups at z = 0.064 and 0.077. The Ly α absorption at 0.064 is particularly dramatic: at this redshift, we find 13 Ly α lines spread over a velocity range of 1000 km s $^{-1}$ with a line-of-sight velocity dispersion of 265 km s $^{-1}$. The second-strongest system at 0.077 is associated with the Abell 559/564 large-scale structure, and this indicates that a filament containing gas and galaxies feeds into the Abell 559/564 supercluster.
- 3. Analysis of the Ly α absorption-line complex at z=0.064 provides strong evidence that the gas is photoionised and relatively cool; we find no compelling evidence of warm-hot gas in this large-scale filament. We detect Si III, Si IV, and C IV in the strongest component in this Ly α complex, and photoionisation models indicate that the gas metallicity is high, [M/H] = -0.05 ± 0.3 . This is somewhat surprising because we do not find any luminous galaxies close to the sight line; the closest galaxy is at a projected distance $\rho=135h_{70}^{-1}$ kpc. The Ly α system at 0.077 is only detected in the C IV doublet, but nevertheless we find a similar result: the lower limit on the metallicity is relatively high ([C/H] > -0.6) while the nearest galaxy is at $\rho=293h_{70}^{-1}$ kpc.
- 4. We have compared the distribution of Ly α Doppler parameters and H I column densities to high-resolution measurements obtained from other sight lines, and we find good agreement. We find that the number of broad Ly α absorbers with $b > 40~{\rm km~s^{-1}}$ per unit redshift is in agreement with results recently reported by Richter et al. (2004,2005) and Sembach et al. (2004). The baryonic content of these broad H I lines is still highly uncertain and requires confirmation with higher S/N data, but it is probable that some of these broad line arise in warm-hot gas and contain an important portion of the baryons in the nearby universe. We also find that the lower bound on b vs. N(H~I) is in agreement with predictions from cosmological simulations.
- 5. The absence of warm-hot gas in the galaxy group/Ly α complex at z=0.064 is difficult to reconcile with X-ray observations of bound galaxy groups. It seems more likely that this in this case we are viewing a large-scale cosmic web filament along its long axis. The filament contains a mix of early- and late-type galaxies and many cool, photoionised clouds.
- 6. The high-metallicity, cool cloud at $z_{\rm abs} = 0.06352$ is probably tidally stripped material. This origin can explain the high metallicity and the lack of hot gas. One of the nearby galaxies has a disturbed morphology consistent with this hypothesis.

Similar clusters of Ly α lines have been observed in other sight lines, and additional examples are likely to be found as we continue to analyse STIS data. We look forward to comparisons of these observations to predictions from cosmological simulations and other theoretical work in order to better understand the processes that affect the evolution of galaxies and the intergalactic medium.

ACKNOWLEDGMENTS

We thank Dan McIntosh and Neal Katz for useful discussions. The STIS observations of HS0624+6907 were obtained for *HST* program 9184 with financial support through NASA grant HST GO-9184.08-A from the Space Telescope Science Institute. This research was also supported in part by NASA through Long-Term Space Astrophysics grant NNG 04GG73G. The *FUSE* data were obtained by the PI team of the NASA-CNES-CSA *FUSE* project, which is operated by Johns Hopkins University with financial support through NASA contract NAS 5-32985. This research has made use of the NASA/IPAC Extragalactic Database (NED), which is operated by the Jet Propulsion Laboratory, California Institute of Technology, under contract with NASA.

REFERENCES

- Allende Prieto, C., Lambert, D. L., & Asplund, A. 2001, ApJ, 556, L63
 Allende Prieto, C., Lambert, D. L., & Asplund, A. 2002, ApJ, 573, L137
 Baugh, C. M., Croton, D. J., Gaztañaga, E., Norberg, P., Colless, M., Baldry, I. K., et al. 2004, MNRAS, 351, L44
- Beers, T. C., Flynn, K., & Gebhardt, K. 1990, AJ, 100, 32
- Bergeron, J., Aracil, B., Petitjean, P. & Pichon, C. 2002, A&A, 396, 11 Bertin, E., & Arnouts, S. 1996, A&AS, 117, 393
- Bowen, D. V., Pettini, M., & Blades, J. C. 2002, ApJ, 580, 169
- Bower, R. G., Lucey, J. R., & Ellis, R. S. 1992, MNRAS, 254, 601
- Bregman, J. N., Dupke, R. A., & Miller, E. D. 2004, ApJ, 614, 31
- Cen, R., & Ostriker, J. P. 1999a, ApJ, 514, 1
- Cen, R. & Ostriker, J. P. 1999, ApJ, 519, L109
- Chen, H.-W., Lanzetta, K. M., Webb, J. K., & Barcons, X. 2001, ApJ, 559, 654
- Chen, H.-W., Marzke, R. O., McCarthy, P. J., Martini, P., Carlberg, R. G., Persson, S. E., Bunker, A., Bridge, C. R., Abraham, R. G. 2003, ApJ, 586, 745
- Colberg, J. M., Krughoff, K. S. & Connolly, A. J. 2005, MNRAS, 359, 272 Colless, M., Dalton, G., Maddox, S., Sutherland, W., Norberg, P., Cole, S., et al. 2001, MNRAS, 328, 1039
- Collins, J. A., Shull, J. M., & Giroux, M. L. 2003, ApJ, 585, 336
- Côté, S., Wyse, R. F. G., Carignan, C., Freeman, K. C., & Broadhurst, T. 2005, ApJ, 618, 178
- Danforth, C. W., & Shull, J. M. 2005, ApJ, 624, 555
- Davé, R., Hernquist, L., Katz, N., & Weinberg, D. H. 1999, ApJ, 511, 521
 Davé, R., Cen, R., Ostriker, J. P., Bryan, G. L., Hernquist, L., Katz, N.,
 Weinberg, D. H., Norman, M. L. & O'Shea, B. 2001, ApJ, 552, 473
- Davé, R. & Tripp, T. M. 2001, ApJ, 553, 528
- Dietrich, J. P., Clowe, D., Schneider, P., Kerp, J. & Romano-Díaz, E. 2004, IAU Symposium, 34
- Doroshkevich, A., Tucker, D. L., Allam, S. & Way, M. J. 2004, A&A, 418, 7
- Edgar, R. J., & Chevalier, R. A. 1986, ApJ, 310, L27
- Einasto, M., Einasto, J., Tago, E., Müller, V., & Andernach, H. 2001, AJ, 122, 2222
- Ferland, G. J., Korista, K. T., Verner, D. A., Ferguson, J. W., Kingdon, J. B. & Verner, E. M. 1998, PASP, 110, 761
- Fox, A. J., Wakker, B. P., Savage, B. D., Tripp, T. M., Sembach, K. R., & Bland-Hawthorn, J. 2005, ApJ, 630, 332
- Futamoto, K., Mitsuda, K., Takei, Y., Fujimoto, R., & Yamasaki, N. Y. 2004, ApJ, 605, 793
- Ganguly, R., Sembach, K. R., Tripp, T. M., & Savage, B. D. 2005, ApJS, 157, 251
- Gray, M. E., Taylor, A. N., Meisenheimer, K., Dye, S., Wolf, C. & Thommes, E. 2002, ApJ, 568, 141
- Haardt, F. & Madau, P. 1996, ApJ, 461, 20
- Heckman, T. M., Norman, C. A., Strickland, D. K., & Sembach, K. R. 2002, ApJ, 577, 691

- Holweger, H. 2001, in AIP Conf. Proc. 598, Solar and Galactic Composition, ed. R. F. Wimmer-Schweingruber (New York: AIP), 23
- Impey, C. D., Petry, C. E., & Flint, K. P. 1999, ApJ, 524, 536
- Jenkins, A., Frenk, C. S., Pearce, F. R., Thomas, P. A., Colberg, J. M., White, S. D. M., Couchman, H. M. P., Peacock, J. A., Efstathiou, G. & Nelson, A. H. 1998, ApJ, 499, 20
- Jenkins, E. B. 1996, ApJ, 471, 292
- Jenkins, E. B., Bowen, D. V., Tripp, T. M., & Sembach, K. R. 2005, ApJ, 623, 767
- Jenkins, E. B., & Tripp, T. M. 2001, ApJS, 137, 297
- Kaldare, R., Colless, M., Raychaudhury, S. & Peterson, B. A. 2003, MN-RAS, 339, 652
- Katz, N., Weinberg, D. H., Hernquist, L., & Miralda-Escudé, J. 1996, ApJ, 457, L57
- Kimble, R. A., Woodgate, B. E., Bowers, C. W., Kraemer, S. B., Kaiser, M. E., Gull, T. R., et al. 1998, ApJ, 492, L83
- Lampton, M., Margon, B., & Bowyer, S. 1976, ApJ, 208, 177
- Landolt, A. U. 1992, AJ, 104, 340
- Lanzetta, K. M., Bowen, D. V., Tytler, D., & Webb, J. K. 1995, ApJ, 442, 538
- Lin, H., Kirshner, R. P., Shectman, S. A., Landy, S. D., Oemler, A., Tucker, D. L., & Schechter, P. L. 1996, ApJ, 464, 60
- Lu, L., Savage, B. D., & Sembach, K. R. 1994, ApJ, 426, 563
- Mac Low, M.-M., & Ferrara, A. 1999, ApJ, 513, 142
- Maller, A. H., McIntosh, D. H., Katz. N., & Weinberg, M. D. 2003, ApJ, 598, L1
- McIntosh, D. H., Zabludoff, A. I., Rix, H.-W., & Caldwell, N. 2005, ApJ, 619, 193
- McKernan, B., Yaqoob, T., & Reynolds, C. S. 2004, ApJ, 617, 232
- Miralda-Escudé, J., Cen, R., Ostriker, J. P., & Rauch, M. 1996, ApJ, 471,
- Moos, H. W., Cash, W. C., Cowie, L. L., Davidsen, A. F., Dupree, A. K., Feldman, P. D., et al. 2000, ApJ, 538, L1
- Moos, H. W., Sembach, K. R., Vidal-Madjar, A., York, D. G., Friedman, S. D., Hébrard, G., Kruk, J. W., et al. 2002, ApJS, 140, 3
- Mulchaey, J. S. 2000, ARA&A, 38, 289
- Mulchaey, J. S., Mushotzky, R. F., Burstein, D., & Davis, D. S. 1996, ApJ,
- Mulchaey, J. S., & Zabludoff, A. I. 1998, ApJ, 496, 73
- Muller, G. P., Reed, R., Armandroff, T., Boroson, T., & Jacoby, G. 1998, SPIE, 3355, 721
- Nicastro, F. et al. 2002, ApJ, 573, 157
- Penton, S. V., Stocke, J. T., & Shull, J. M. 2002, ApJ, 565, 720
- Press, W. H., Teukolsky, S. A., Vetterling, W. T., & Flannery, B. P. 1992, Numerical Recipes in Fortran (2nd ed.; Cambridge: Cambridge Univ. Press)
- Prochaska, J. X., Chen, H.-W., Howk, J. C., Weiner, B. J., & Mulchaey, J. 2004, ApJ, 617, 718
- Prochaska, J. X., Gawiser, E., Wolfe, A. M., Cooke, J., & Gelino, D. 2003, ApJS, 147, 227
- Richter, P., Savage, B. D., Sembach, K. R., & Tripp, T. M. 2005, A&A, submitted
- Richter, P., Savage, B. D., Tripp, T. M. & Sembach, K. R. 2004, ApJS, 153, 165
- Rines, K., Mahdavi, A., Geller, M. J., Diaferio, A., Mohr, J. J. & Wegner, G. 2001, ApJ, 555, 558
- Savage, B. D., Lehner, N., Wakker, B. P., Sembach, K. R., & Tripp, T. M. 2005, ApJ, 626, 776
- Savage, B. D. & Sembach, K. R. 1991, ApJ, 379, 245
- Savage, B. D., Sembach, K. R., Tripp, T. M., & Richter, P. 2002, ApJ, 564, 631
- Scharf, C., Donahue, M., Voit, G. M., Rosati, P. & Postman, M. 2000, ApJ, 528, L73
- Schaye, J., Aguirre, A., Kim, T.-S., Theuns, T., Rauch, M., & Sargent, W. L. W. 2003, ApJ, 596, 768
- Schmutzler, T., Tscharnuter, W.M. 1993, A&A, 273, 318
- Sembach, K. R., Savage, B. D., Lu, L., Murphy, E. M. 1995, ApJ, 451, 616
- Sembach, K. R., Savage, B. D., Lu, L., Murphy, E. M. 1999, ApJ, 515, 108

- Sembach, K. R., Howk, J. C., Savage, B. D., & Shull, J. M. 2001, AJ, 121, 992
- Sembach, K. R., Tripp, T. M., Savage, B. D. & Richter, P. 2004a, ApJS, 155, 351
- Sembach, K. R., Wakker, B. P., Tripp, T. M., et al. 2004b, ApJS, 150, 387
- Shapiro, P. R., & Moore, R. T. 1976, ApJ, 207, 460
- Sheinis, A. I., Bolte, M., Epps, H. W., Kibrick, R. I., Miller, J. S., Radovan, M. V., Bigelow, B. C., & Sutin, B. M. 2002, PASP, 114, 851
- Shull, J. M., Penton, S. V., Stocke, J. T., Giroux, M. L., van Gorkom, J. H., Lee, Y. H., & Carilli, C. 1998, AJ, 116, 2094
- Shull, J. M., Roberts, D., Giroux, M. L., Penton, S. V., & Fardal, M. A. 1999, AJ, 118, 1450
- Shull, J. M., Tumlinson, J., & Giroux, M. L. 2003, ApJ, 594, 107
- Stocke, J. T., Shull, J. M., Penton, S., Donahue, M., & Carilli, C. 1995, ApJ, 451, L75
- Stoughton, C., Lupton, R. H., Bernardi, M., Blanton, M. R., Burles, S., Castander, F. J., et al. 2002, AJ, 123, 485
- Strickland, D. K., Heckman, T. M., Colbert, E. J. M., Hoopes, C. G., & Weaver, K. A. 2004, ApJS, 151, 193
- Sutherland, R. S. & Dopita, M. A. 1993, ApJS, 88, 253
- Tittley, E. R. & Henriksen, M. 2001, ApJ, 563, 673
- Tripp, T. M., Bowen, D. V., Sembach, K. R., Jenkins, E. B., Savage, B. D., & Richter, P. 2004, in Astrophysics in the Far Ultraviolet: Five Years of Discovery with *FUSE*, eds. G. Sonneborn, H. W. Moos, & B.-G. Andersson (San Francisco: ASP), in press (astro-ph/0411151)
- Tripp, T. M., Giroux, M. L., Stocke, J. T., Tumlinson, J. & Oegerle, W. R. 2001, ApJ, 563, 724
- Tripp, T. M., Jenkins, E. B., Bowen, D. V., Prochaska, J. X., Aracil, B. & Ganguly, R. 2005, ApJ, 619, 714
- Tripp, T. M., Lu, L., & Savage, B. D. 1998, ApJ, 508, 200
- Tripp, T. M., & Savage, B. D. 2000, ApJ, 542, 42
- Tripp, T. M., Savage, B. D., & Jenkins, E. B. 2000, ApJ, 534, L1
- Tripp, T. M., Wakker, B. P., Jenkins, E. B., Bowers, C. W., Danks, A. C., Green, R. F., Heap, S. R., Joseph, C. L., Kaiser, M. E., Linsky, J. L. & Woodgate, B. E. 2003, AJ, 125, 3122
- Voit, G. M. 2005, RvMP, 77, 207
- Wakker, B. P., Oosterloo, T. A., & Putman, M. E. 2002, AJ, 123, 1953
- Wang, Q. D., Connolly, A. & Brunner, R. 1997, ApJ, 487, L13
- Weymann, R. J., Vogel, S. N., Veilleux, S. & Epps, H. W. 2001, ApJ, 561, 559
- Webb, J. K. 1987, PhD thesis, Univ. Cambridge
- Williger, G. M., Heap, S. R., Weymann, R. J., Davé, R., Ellingson, E., Carswell, R. F., Tripp, T. M., & Jenkins, E. B. 2005, ApJ, in press (astro-ph/0505586)
- Wolfire, M. G., McKee, C. F., Hollenbach, D., & Tielens, A. G. G. M. 1995, ApJ, 453, 673
- Woodgate, B. E., Kimble, R. A., Bowers, C. W., Kraemer, S., Kaiser, M. E., Danks, A. C., et al. 1998, PASP, 110, 1183
- Yuan, Q., Green, R. F., Brotherton, M., Tripp, T. M., Kaiser, M. E., & Kriss, G. A. 2002, ApJ, 575, 687
- Zabludoff, A. I., & Mulchaey, J. S. 1998, ApJ, 496, 39